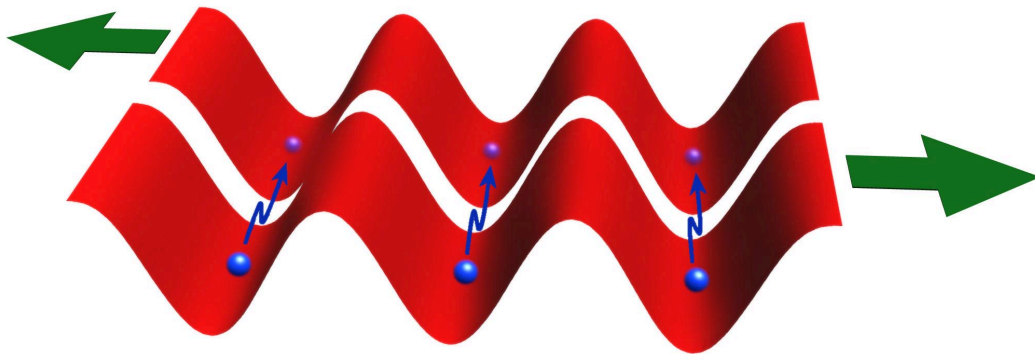# Chapter 6

Chaos-Assisted Tunneling

6.1   Overview

We will now discuss experimental results on quantum dynamics in the case where the corresponding classical description is characterized by a mixed phase space, in which chaotic and stable regions coexist. This regime is distinctly different from the strongly chaotic regime of Chapter 4, and the study of this new regime is enabled by the state-preparation methods outlined in the previous chapter. The experiments study the atomic motion in a standing wave of light that is modulated sinusoidally in time. In particular, we will focus on tunneling between two islands of stability in the classical phase space of this system. Because the classical transport between the islands is forbidden by the system dynamics and not by a potential barrier, this tunneling is known as *dynamical tunneling*. We will investigate the salient details of the tunneling, including how the tunneling depends on the phase-space location of the initial condition and the role of symmetry in supporting the tunneling. More significantly, though, we will discuss how the presence of chaos in phase space can enhance the tunneling rate, and we will examine evidence for such *chaos-assisted tunneling* in the experimental results. This evidence includes a comparison to a dynamical tunneling process (Bragg scattering) that occurs in the integrable counterpart to the modulated system; a fast, secondary oscillation in the tunneling dynamics; and the dependence of the tunneling rate on the lattice intensity. Finally, we will see how noise destroys the quantum tunneling effect and restores classical-like behavior, and how the system is more sensitive to noise as the parameters move the dynamics closer to the classical limit.

A subset of the data presented here, including the observation of tunneling oscillations, the effects of location in phase-space and broken symmetry, a comparison to Bragg scattering, and the influence of a third (chaotic) state has been previously published in [Steck01].

6.2   Barrier Tunneling

Before tackling the issue of tunneling in phase space, we will begin with the familiar problem of tunneling in a symmetric double-well potential, of which one example is shown in Fig. 6.1. In the limit where the barrier separating the wells is arbitrarily high, the system can be regarded as two isolated, identical potential wells, and thus the level structure of the combined system is a

set of degenerate doublets. For a potential barrier of finite height, the doublet states are coupled because a state localized in one well "leaks" through the barrier and into the other well. In the weak-coupling regime, we can neglect the coupling of a particular doublet to other doublets, and thus the Hamiltonian for a doublet can be written as

$$H = \begin{pmatrix} E_0 & -\wp/2 \\ -\wp/2 & E_0 \end{pmatrix} \tag{6.1}$$

in the uncoupled basis $\{|L\rangle, |R\rangle\}$ (localized in the left and right well, respectively), where $\wp/2$ represents the coupling energy between the two states. The coupling matrix elements in this case are negative because the perturbation is a reduction of the potential from an arbitrarily large height. The eigenvalues of this Hamiltonian are $E_0 \pm \wp/2$, and the eigenvectors are the symmetric and antisymmetric combinations $(|L\rangle \pm |R\rangle)/\sqrt{2}$ of the uncoupled states. The antisymmetric state has the larger energy for positive $\wp$, which is consistent with the small-barrier limit of a single well. The lowest energy doublet for the quartic double well is shown in Fig. 6.1.

The doublet of a symmetric and an antisymmetric state can then fully describe the tunneling behavior. If we begin the evolution with a state localized in the left-hand well, it
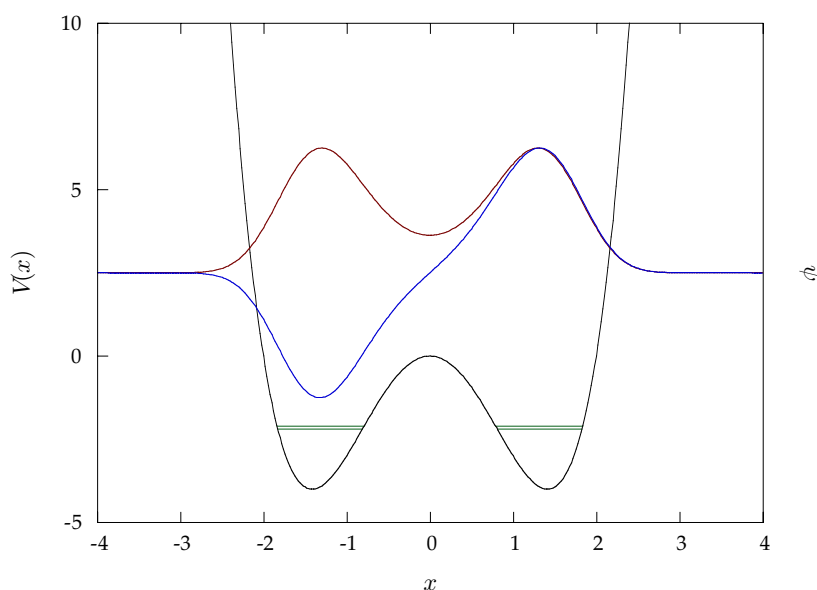

Figure 6.1: The ground-state tunneling doublet of the quartic double well potential, $H = p^2/2 + x^4 - 4x^2$ (with $\hbar = 1$). The symmetric-state energy is -2.20, and the antisymmetric-state energy is -2.10.

can be written approximately as the superposition $(|+\rangle + |-\rangle)/\sqrt{2}$, where $|+\rangle$ and $|-\rangle$ are the symmetric and antisymmetric doublet states, respectively. The time-dependent solution is

$$
\begin{aligned}
|\psi(t)\rangle &= \frac{1}{\sqrt{2}}\left(|+\rangle e^{i\wp t/2\hbar} + |-\rangle e^{-i\wp t/2\hbar}\right) \\
&= \cos\left(\frac{\wp t}{2\hbar}\right)|\mathrm{L}\rangle + i\sin\left(\frac{\wp t}{2\hbar}\right)|\mathrm{R}\rangle \ ,
\end{aligned}
\tag{6.2}
$$

up to an overall phase. Thus, as the two states dephase, the wave packet oscillates between the two wells with an angular frequency of $\wp/\hbar$. In the WKB (semiclassical) approximation, the tunnel splitting $\wp$ can be written [Landau77; Tomsovic94; Brack97]

$$
\wp = \frac{\hbar\omega_0}{\pi} \exp\left(-\frac{1}{\hbar}\int_{x_1}^{x_2}\sqrt{2m(V(x) - E_0)}\,dx\right) \ ,
\tag{6.3}
$$

where x_1 and x_2 are the two inner classical turning points at energy E_0, and ω_0 is the classical angular oscillation frequency in one of the uncoupled wells. This $A\exp(-S/\hbar)$ scaling of the tunneling rate with $\hbar$, where A is a smooth function of $\hbar$ and S is the imaginary part of the classical action along a (complex) path connecting the two tunneling regions, is characteristic of tunneling where only two states are involved [Tomsovic94; Creagh98].

It is important to note that the tunneling here is facilitated by the reflection symmetry of the system. In a double well with small asymmetry (i.e., the energy difference between the wells is small compared to the uncoupled energy splittings), we can simply change the model Hamiltonian (6.1) to reflect an energy displacement of one well:

$$
H = \begin{pmatrix} E_0 + \Delta & -\wp/2 \\ -\wp/2 & E_0 \end{pmatrix} \ .
\tag{6.4}
$$

In this model, Δ controls the asymmetry of the system. Comparing this Hamiltonian to the Hamiltonian (2.25) for a driven two-level atom in the rotating-wave approximation, we see that these two systems are formally equivalent. Thus the eigenvalues are

$$
E_\pm = E_0 + \frac{1}{2}\left(\Delta \mp \sqrt{\Delta^2 + \wp^2}\right) \ ,
\tag{6.5}
$$

and the corresponding eigenvectors are

$$
\begin{aligned}
|+\rangle &= \sin\theta|\mathrm{L}\rangle + \cos\theta|\mathrm{R}\rangle \\
|-\rangle &= \cos\theta|\mathrm{L}\rangle - \sin\theta|\mathrm{R}\rangle \ ,
\end{aligned}
\tag{6.6}
$$

where

$$\sin\theta = \sqrt{\frac{1}{2}\left(1 - \frac{\Delta}{\sqrt{\Delta^2 + \wp^2}}\right)}$$

$$\cos\theta = \sqrt{\frac{1}{2}\left(1 + \frac{\Delta}{\sqrt{\Delta^2 + \wp^2}}\right)} \ , \tag{6.7}$$

or more compactly,

$$\tan(2\theta) = -\frac{\wp}{\Delta} \quad \left(0 \leq \theta < \frac{\pi}{2}\right) \ . \tag{6.8}$$

As in the two-level atom, the $|+\rangle$ and $|-\rangle$ states are the "dressed" states of the system, and the tunneling oscillations can be regarded as Rabi oscillations between the two wells. The asymmetry in the double well then corresponds to driving a two-level atom off resonance, and the coupling induces an avoided crossing of the two levels as a function of Δ, as illustrated in Fig. 6.2. In the asymmetric case, the eigenstates lose their symmetric and antisymmetric characters, reducing to the uncoupled states in the limit of large Δ. The tunneling proceeds at the generalized
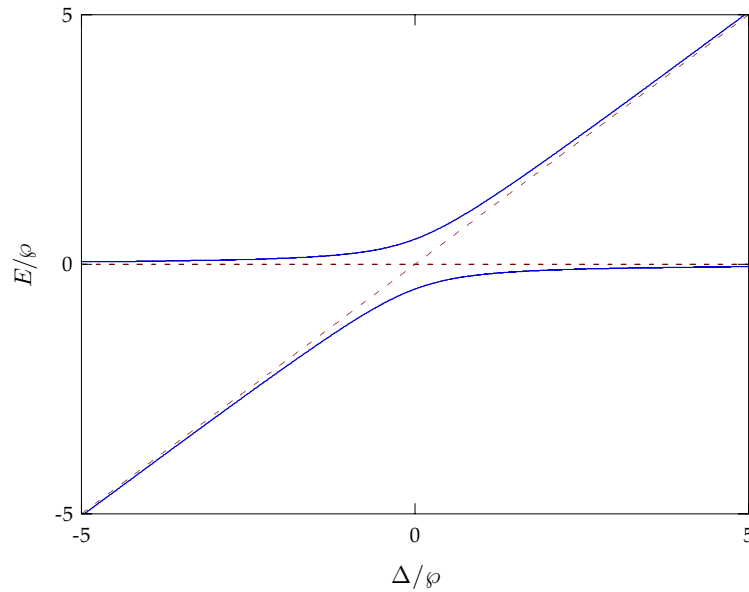

Figure 6.2: Illustration of an avoided crossing of a tunneling doublet as a function of the asymmetry parameter Δ, as described by Eq. 6.5. The dashed lines show the energies in the absence of any coupling.

Rabi frequency $\sqrt{\wp^2 + \Delta^2}$, which is faster than in the symmetric case, but the tunneling is suppressed in the sense that only a fraction $\wp^2/(\wp^2 + \Delta^2)$ of the population in the initial well participates in the coherent tunneling oscillation. Hence, the symmetry is an important ingredient for producing the tunneling. For larger asymmetries, a state in one well may couple to a different state in the other well, causing this picture to break down; such "accidental" degeneracies can also lead to tunneling, even in the absence of symmetry.

6.3   Dynamical Tunneling

In the case of the double-well potential, the potential barrier is an obvious impediment to the classical transport between the two wells. However, it is useful to regard the classical transport more abstractly, from the point of view of the phase space of the double well, as shown in Fig. 6.3. Here the two wells are represented by regions surrounding stable (elliptic) fixed points. Classical trajectories within a single well are confined to nearly elliptical trajectories surrounding only one of the fixed points, while trajectories with enough energy to cross the potential barrier are represented by larger contours that surround both of the elliptic points. We can thus view these invariant surfaces along which the trajectories lie (which correspond to KAM surfaces in
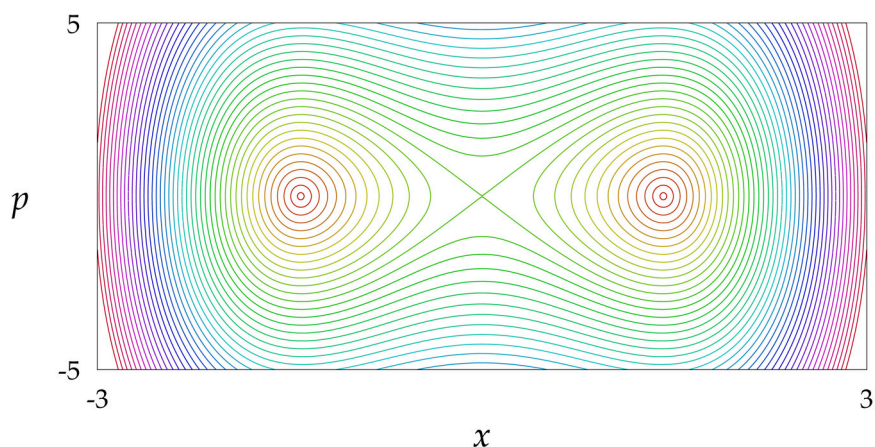

Figure 6.3: Phase space for the quartic double-well potential in Fig. 6.1. The barrier tunneling can be regarded as tunneling between classical invariant tori associated with the two wells. Classical transport between the wells is forbidden because the classical trajectories are confined along these invariant surfaces.

near-integrable systems) as barriers for the classical transport, because classical trajectories cannot cross these surfaces. This is true in a trivial sense for the double well, because all trajectories are confined to their corresponding surfaces. However, these invariant surfaces retain their role as barriers for classical transport in all systems with two degrees of freedom (or, equivalently, periodically driven systems with one degree of freedom), even when the system is not integrable. Trajectories can wander freely throughout chaotic regions, but invariant surfaces (including KAM surfaces, which survive in the presence of weak, nonintegrable perturbations) divide the phase space and cannot be crossed by any trajectory, as a consequence of the continuity and the deterministic character of the equations of motion. This is not true in systems with $N > 2$ degrees of freedom, because the N-dimensional invariant surfaces no longer partition the $(2N - 1)$-dimensional surfaces of constant energy (thus allowing for Arnol'd diffusion [Reichl92]). For the systems that we will consider here, though, we can regard these invariant surfaces as being the fundamental barriers in phase space to classical transport.

Invariant surfaces are common in nearly integrable systems, and a potential barrier is not necessary for their existence. Davis and Heller first pointed out that *dynamical tunneling* could occur between two separated, symmetry-related stable regions in phase space, where the classical transport is forbidden by the dynamics and not by a potential barrier [Davis81]. They considered tunneling between two types of oscillatory motion, which corresponds to tunneling between two islands of stability in phase space, in a two-dimensional, nonlinear potential with a reflection symmetry. Tunneling can also occur between other types of stable regions in phase space, such as bands of KAM surfaces in the phase space of the annular billiard [Doron95].

In fact, the two essential ingredients for tunneling are the existence of a discrete symmetry and the separation of the (quasi)energy eigenstates in phase space [Chirikov95]. The second ingredient is obviously fulfilled in the barrier-tunneling problem, because the low-energy states in the two wells are localized in their respective wells. In dynamical tunneling between two islands of stability, states are also localized in the islands, which support states similar to harmonic-oscillator states [Scharf92] (as one might expect from EBK quantization). As we have seen before, though, localization is natural in quantum nonlinear systems even with widespread

chaos. Thus, there is also the possibility of "retunneling" [Sridhar92] between quantum local-ized states in the Sinai billiard. Here, the transport is forbidden by quantum localization (but not classically), but oscillatory transport occurs anyway across this quantum "barrier." A simi-lar tunneling effect can occur between symmetry-related, exponentially localized states in the kicked rotor [Casati94].

Previous experimental work in the area of dynamical tunneling has been restricted to spectroscopic observation of tunneling doublets. It has been pointed out [Frederick88; Heller91] that the experimental fluorescence-excitation spectrum of the benzophenone molecule in [Holtzclaw86] shows doublet features that correspond to dynamical tunneling. In this molecule, there are two symmetry-related benzene rings, each of which can undergo twisting motions. The tunneling is between the two "local modes," where one ring twists while the other is at rest; the spectral doublets then correspond to the symmetric and antisymmetric combinations of the lo-cal modes. There is also experimental evidence for dynamical tunneling in wave analogies to quantum mechanics. The tunneling doublets have also been directly observed in the resonance spectroscopy of a microwave-cavity realization of the annular billiard [Dembowski00]. Further-more, the Shnirelman peak [Chirikov95] in the level spacing distribution is a similar signature of dynamical tunneling, and has recently been observed in an acoustical resonator [Neicu01] and a microwave-cavity experiment [Koch01]. Finally, there is an experimental effort, complemen-tary to the one described here, to study dynamical tunneling of a Bose-Einstein condensate in an amplitude-modulated standing wave of light [Hensinger01]. This experiment, while being similar in some respects to the experiments described below, considers tunneling between a dif-ferent pair of resonances (second-order resonances [Dyrting93]) than we consider later in this chapter.

6.3.1   Tunneling in Atom Optics

The basic experimental system that we used to study tunneling is very similar to that used in the kicked-rotor experiments in Chapter 4 (save for the substantially more complicated quantum-state preparation), the primary difference being the temporal dependence of the potential. To

produce a more manageable, mixed classical phase space, the amplitude modulation of the potential was relatively smooth:

$$H = \frac{p^2}{2m} - 2V_0 \cos^2\left(\frac{\pi t}{T}\right) \cos(2k_{\mathrm{L}}x) \ .$$

(6.9)

The quantities here are as they were defined in Chapter 4. This Hamiltonian is again that of the pendulum, but with a sinusoidal variation of the potential amplitude in time from zero to $2V_0$ with period T. We can make a transformation into scaled units that is similar to the transformation used for the kicked rotor, since this system is effectively a kicked rotor with long, sinusoidal pulses:

$$
\begin{aligned}
x' &= 2k_{\mathrm{L}}x \\
p'/\hbar &= p/2\hbar k_{\mathrm{L}} \\
t' &= t/T \\
H' &= (\hbar T/\hbar)H \\
\alpha &:= (\hbar T/\hbar)V_0 \\
\hbar &:= 8\omega_{\mathrm{r}}T \ .
\end{aligned}
$$

(6.10)

Here, we have chosen the time scaling so that the scaled period of the modulation is unity, α is the scaled amplitude of the potential (related to the amplitude in pendulum units by $\alpha = \hbar^2\alpha_{\mathrm{p}}$), and $\hbar$ is again the effective Planck constant in the scaled units. The Hamiltonian in scaled units, after dropping the primes, is

$$H = \frac{p^2}{2} - 2\alpha \cos^2(\pi t) \cos(x) \ ,$$

(6.11)

with the Schrödinger equation given by $H\psi = i\hbar\partial_t\psi$.

In the spirit of the analysis of Section 4.4.4, we can rewrite the potential as

$$V(x,t) = -\alpha \cos(x) - \frac{\alpha}{2} \cos(x + 2\pi t) - \frac{\alpha}{2} \cos(x - 2\pi t) \ .$$

(6.12)

In this form, the potential appears as the sum of three pendulum-like terms with time-independent amplitude. Thus the modulated potential can be regarded as a combination of three pendulum potentials; two of these potentials are moving with momentum $\pm 2\pi$, and the third is stationary. When this system is sampled at integer times, these three terms produce primary resonances in phase space centered at $(x, p) = (0, \pm 2\pi)$ and $(0, 0)$. This structure is evident in the phase spaces in Appendix C, especially for small α. For larger α, the resonances interact,

producing a phase-space structure of bands of chaos surrounding the three main islands of stability. The tunneling that we consider here is between the two outer islands of stability, which are related to each other by reflection symmetry through the origin $(x, p) = (0, 0)$. In configuration space, the tunneling occurs between a state of coherent motion in only one direction to a state of the oppositely directed motion. These two states each correspond to being tightly bound to one of the two moving components of the lattice. The center island does not directly participate in the tunneling.

To observe tunneling in the experiment, we used the state-preparation procedure described in Chapter 5. This procedure produced an initial state centered on one of the outer resonances with narrow slices taken out of the overall Gaussian profile (because of the narrow Raman velocity selection). A schematic representation of the initial condition for $\bar{k} = 2.08$ (corresponding to a 20 μs modulation period) and an 800 μs Raman-pulse duration is shown in Fig. 6.4 with the classical phase space for the experimental value of $\alpha = 10.5$. In this strongly driven regime, the center island has mostly dissolved into the chaotic sea, making this a clean regime for studying tunneling between the remaining two islands. The two islands are located $8 \cdot 2\hbar k_{\text{L}}$ apart in momentum. The measured evolution of the momentum distribution in this case is plotted in Fig. 6.5, where the distribution was sampled every 2 modulation periods out to 80 periods. Four of these distributions are also shown in more detail in Fig. 6.6. Four coherent oscillations of the atoms between the islands are apparent before the transport is damped out. During the first oscillation, nearly half of the atoms appear in the secondary (tunneled) peak.

At this point, a few words are in order concerning the initial condition plotted in Fig. 6.4. The ellipses shown are the 50% contours of the atomic distribution in phase space. This depiction represents a classical distribution with the same x and p marginal distributions as the Wigner function for the initial state, but is not itself the correct Wigner function. The proper Wigner function for this state is more complicated, and can be constructed from the plotted distribution as follows. Whereas the distribution shown has momentum slices spaced by $\bar{k}$, the Wigner function has additional (positive) slices within the Gaussian profile between these slices, so that the spacing is $\bar{k}/2$. This combined structure is then repeated a distance π away in position,
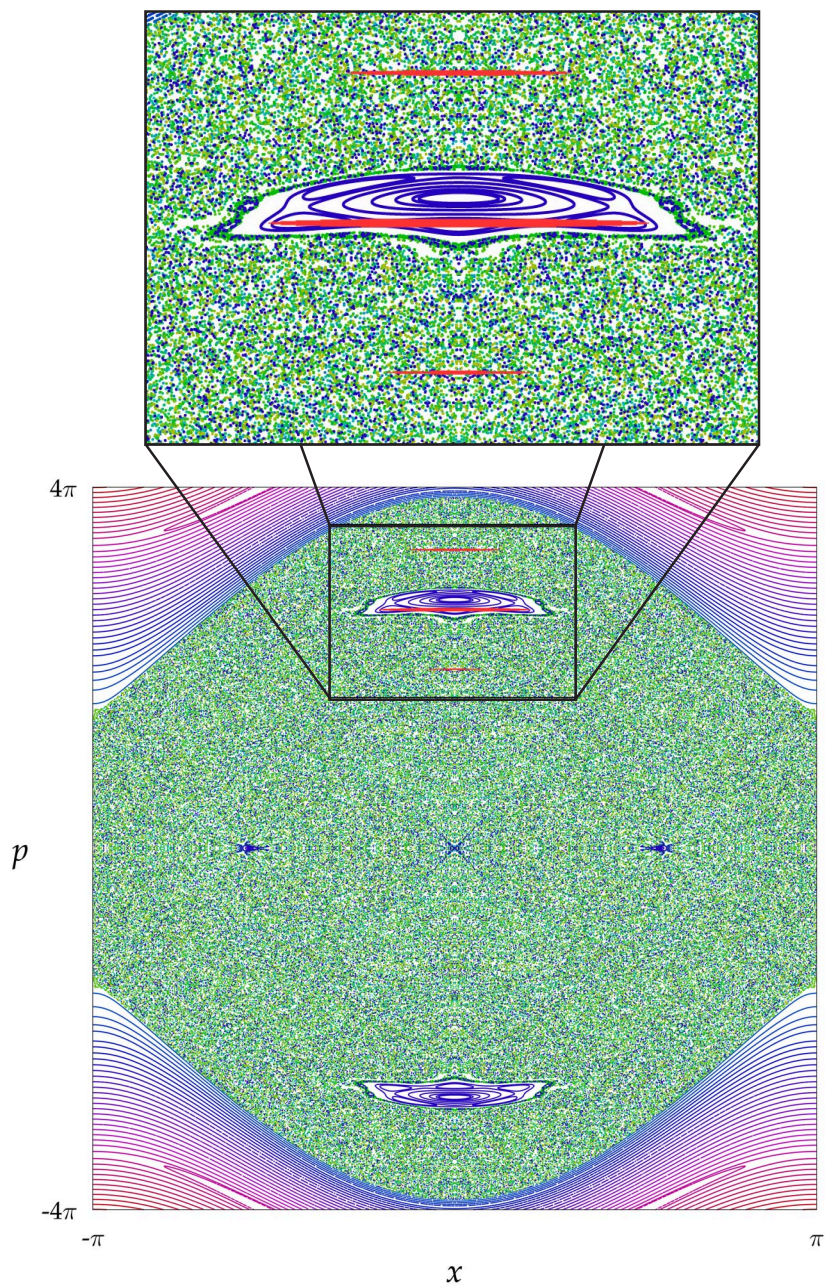
Figure 6.4: Phase space corresponding to the experimental conditions for the data in Fig. 6.5 ($\alpha = 10.5$). A schematic representation of the atomic initial state is superimposed in red on the upper island ($\bar{k} = 2.08$), showing the subrecoil structure that we expect from the state-preparation procedure. A magnified view of the upper island and initial quantum state is also shown.
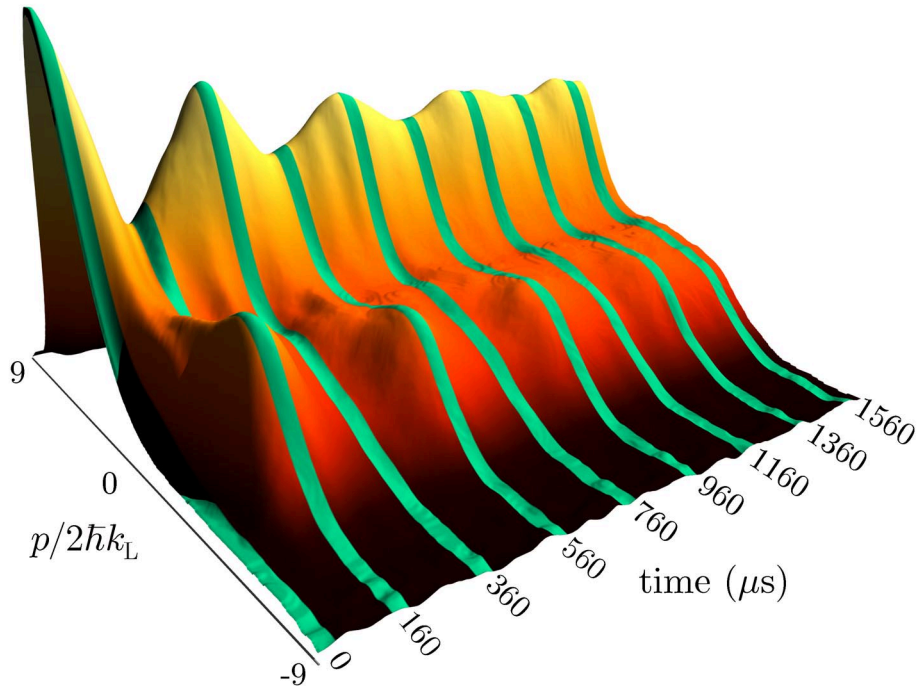
Figure 6.5: Observation of coherent tunneling oscillations in the momentum-distribution evolution between the two symmetry-related islands of stability, as shown in Fig. 6.4. The two island centers are separated in momentum by $8 \cdot 2\hbar k_{\mathrm{L}}$. In this plot, the distribution was sampled every 40 μs (every 2 modulation periods). Each of the distributions represent averages over 20 iterations of the experiment.
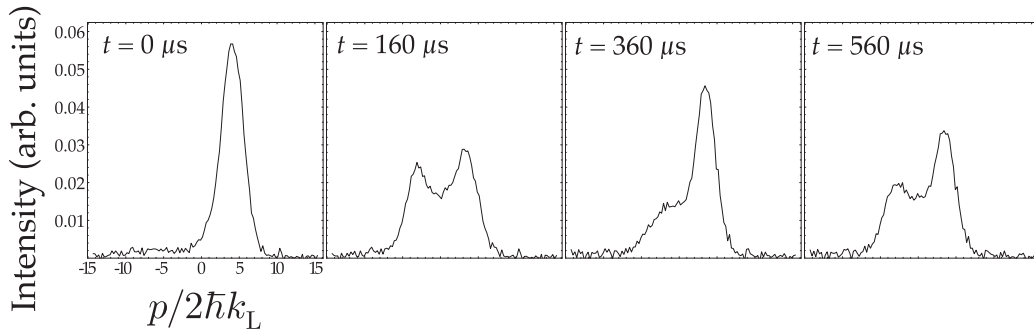

Figure 6.6: Detailed view of the first four highlighted distributions in Fig. 6.5, where it is clear that a significant fraction of the atoms tunnel to the other island. The distributions here were averaged over 100 iterations of the experiment.

except that the slices added to the original three have negative amplitude in this new group. The population $\hbar/2$ away from the center of the wave packet integrates to zero when computing the p marginal distribution, and the population is only in the vicinity of the island when computing the x marginal distribution. These extra structures represent coherence of the wave packet over multiple wells of the potential, where the coherence length scales as the inverse of the width of the narrow slices. Finally, we note that the initial condition plotted here assumes a minimum-uncertainty Gaussian, but in the experiment the wave packet was distorted slightly by anharmonic evolution in the lattice during the state preparation.

6.3.2 Broken Symmetry

The subrecoil Raman velocity selection is important not only to produce a nearly uncertainty-limited wave packet, but also in order to satisfy a quantum symmetry required to observe tunneling. This symmetry stems from the discrete translational symmetry of the potential, as discussed in Chapter 2, which causes momentum transitions to occur in discrete steps of $\hbar$ (or $2\hbar k_\mathrm{L}$ in unscaled units). Thus the momentum state $|n\hbar + \delta\rangle$ (where n is an integer) is coupled to the $|-n\hbar + \delta\rangle$ state via 2-photon transitions. For $0 < |\delta| < \hbar/2$, these states are therefore not coupled to their symmetric reflections about $p = 0$. In the language of the double-well potential above, this situation is equivalent to an asymmetric double well, because the potential couples two states with a difference of $2n\hbar\delta$ in energy. Thus, complete tunneling only fully occurs for the $|n\hbar\rangle$ momentum states and is suppressed for states off this integer ladder. A deviation in momentum from this symmetric ladder is equivalent to a broken time-reversal symmetry [Casati94], and the symmetric/antisymmetric doublet character can be sensitive to this broken symmetry [Chirikov95]. This symmetry condition is automatically fulfilled for a rotor, because the periodic boundary conditions select the tunneling states, but in the case of a particle in an extended potential, as in the present experiment, careful state preparation is required to populate only the proper states. Thus the subrecoil velocity selection, coupled with the rest of the state-preparation sequence, fulfills the simultaneous goals of producing a wave packet localized on an island of stability and populating only states with momentum nearly an integer multiple of $\hbar$.

The importance of the subrecoil momentum selection is demonstrated in Fig. 6.7, where the evolution of $\langle p \rangle$ corresponding to the data in Fig. 6.5 (with an 800 μs Raman selection pulse) is shown, along with data for 400 and 200 μs Raman pulses. Shorter Raman pulses result in wider velocity slices, so that fewer of the atoms fulfill the symmetry condition, and thus the tunneling oscillations are suppressed as the Raman pulse duration decreases. Also shown is the case where the experiment was performed without any Raman velocity selection, and the state-preparation sequence in the 1D lattice was performed immediately after cooling in the 3D lattice. The momentum distribution after the atoms were released from the 3D lattice was not subrecoil, so the prepared wave packet was no longer minimum uncertainty (the wave-packet
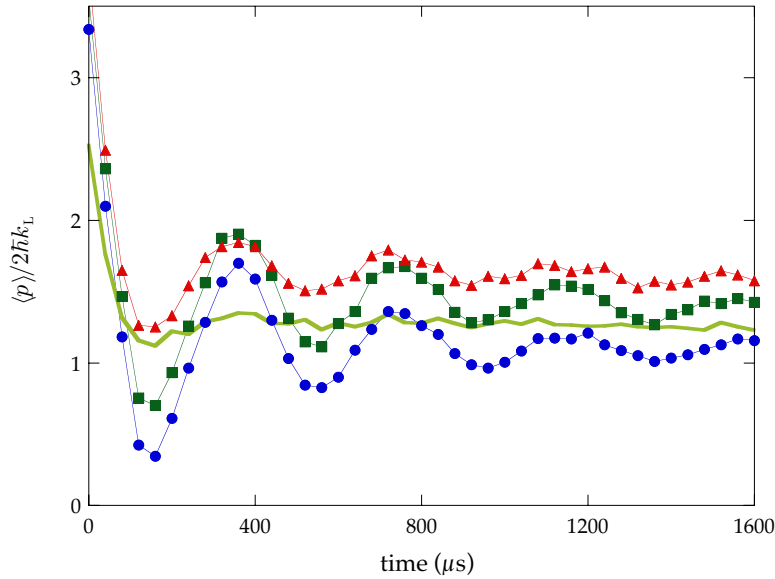

Figure 6.7: Comparison of tunneling oscillations for different Raman π-pulse durations, and thus selected velocity widths ($\alpha = 10.5$, $\tilde{k} = 2.08$). The strongest oscillations shown here (circles) correspond to the longest (800 μs) Raman velocity selection pulse used, which implies a momentum slice with a HWHM of $0.03 \cdot 2\hbar k_{\mathrm{L}}$. The data here are derived from the momentum distributions in Fig. 6.5. Also shown are data for a 400 μs selection pulse (corresponding to a HWHM of $0.06 \cdot 2\hbar k_{\mathrm{L}}$) and a 200 μs selection pulse (corresponding to a HWHM of $0.12 \cdot 2\hbar k_{\mathrm{L}}$), illustrating the reduced contrast in the tunneling oscillations as the pulse duration is decreased. The heavy solid line corresponds to a measurement where no Raman velocity selection was performed, but the atoms were subjected to the state-preparation sequence after cooling in the 3D lattice (where they have a HWHM in momentum of $0.8 \cdot 2\hbar k_{\mathrm{L}}$). The tunneling oscillations are completely suppressed in this last case. The data were averaged over 20 (800 μs tag), 10 (400 μs tag), 5 (200 μs tag), and 1 (no Raman tag) iterations of the experiment.

area in phase space was about three times the size of a minimum-uncertainty state). More importantly, though, there was no subrecoil structure in this last case, so that the tunneling oscillations are completely absent in the figure. The evolution of the momentum distribution in this case is shown in Fig. 6.8. There is perhaps a half of a tunneling oscillation at the beginning of the evolution, but the oscillations are again clearly suppressed. Most of the atoms have suppressed tunneling amplitudes, because they are too far away from the proper tunneling momenta. Also, because there is a continuum of states populated near the symmetric ladder, the different momentum classes tunnel at slightly different rates. This situation provides another mechanism for damping of the coherent oscillations, similar to broadened excitation of a two-level atom.

We also studied this broken symmetry more directly by fixing the velocity-selection width at the minimum value and varying the locations of the velocity slices within the Gaussian profile. This was accomplished easily by slightly varying the detuning of the Raman pulse before
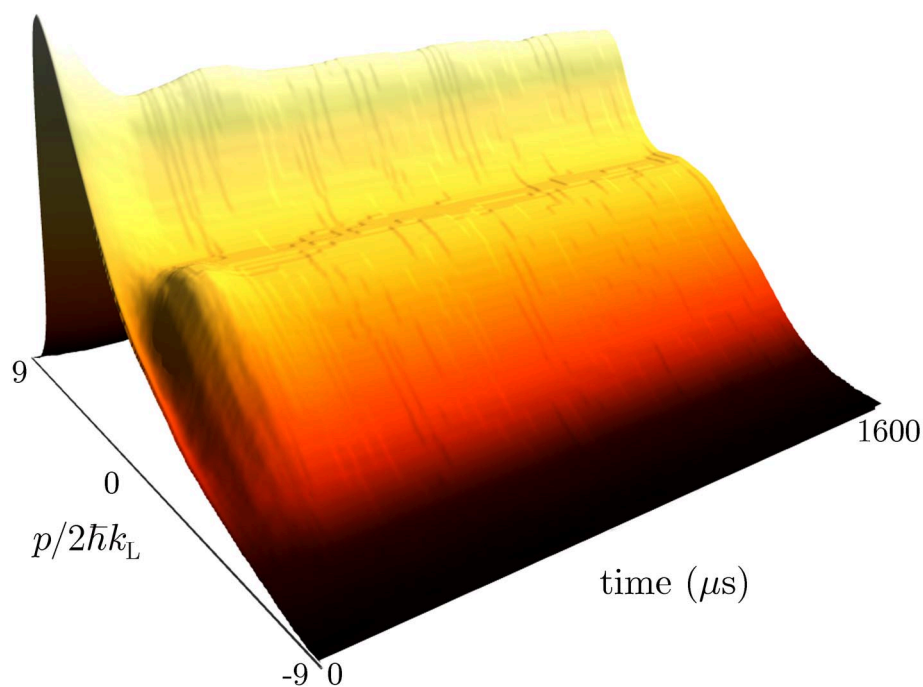

Figure 6.8: Evolution of the momentum distribution as in Fig. 6.5, but without Raman velocity selection. The tunneling oscillations are clearly suppressed here.

loading the atoms into the standing wave. The experimental results are shown in Fig. 6.9, where the data with the optimum Raman detuning are compared to data with two other Raman detunings. As the detuning increases, the tunneling oscillations are again suppressed, being almost fully destroyed for an offset corresponding to $0.12 \cdot 2\hbar k_{\mathrm{L}}$ in momentum. The tunneling is thus quite sensitive to this broken symmetry.

Fig. 6.10 shows simulations of the tunneling oscillations that model the Raman tag widths in Fig. 6.7 as well as oscillations in the limit of arbitrarily narrow velocity selection (i.e., the rotor case). The simulation assumes an overall profile of a minimum-uncertainty wave packet with the same center and momentum width as in the experiment, along with ideal Raman π-pulse momentum-selection profiles. With no width, there are no signs of damping, and the tunneling is nearly complete. With wider momentum slices, a smaller fraction of the atoms successfully tunnels, and the tunneling oscillations become increasingly damped. The Raman tagging thus explains a substantial part of the incomplete tunneling and damping in the exper-
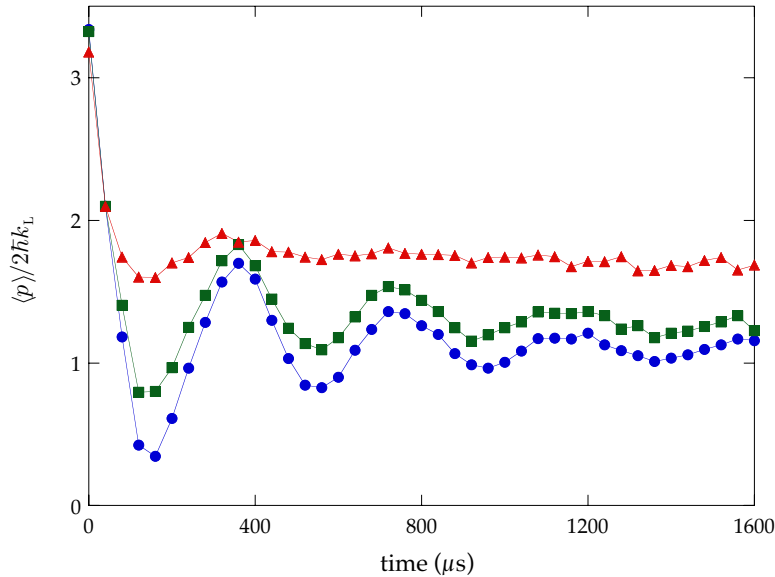

Figure 6.9: Comparison of tunneling oscillations for different Raman detunings ($\alpha = 10.5$, $\bar{k} = 2.08$). The strongest oscillations observed (circles) correspond to Raman velocity selection at $p = 0$. The other two cases are for velocity selection at $p = 0.05 \cdot 2\hbar k_{\mathrm{L}}$ (squares), where the oscillations are partially suppressed, and $p = 0.12 \cdot 2\hbar k_{\mathrm{L}}$ (triangles), where the oscillations are almost completely suppressed.

iment. In principle, then, a Raman tagging pulse even longer than 800 μs could have provided more complete tunneling, although such a pulse was impractical, as the atoms would have fallen too far with respect to the beams over the course of the experimental sequence.

Finally, the reader may have noticed that the average momenta $\langle p \rangle$ in the experimental plots are reduced in magnitude compared to what one might expect. This is especially evident at the beginning of the evolution, where the average momentum appears to be around $3.3 \cdot 2\hbar k_{\mathrm{L}}$, even though the distribution is peaked at $4.1 \cdot 2\hbar k_{\mathrm{L}}$. This effect is an artifact of the reduction of the distributions to average values, where the broad backgrounds of the distributions and the truncation at large momenta (the $\bar{k} = 2.08$ data are truncated beyond $\pm 9 \cdot 2\hbar k_{\mathrm{L}}$ and the $\bar{k} = 1.04$ data are truncated beyond $\pm 14.1 \cdot 2\hbar k_{\mathrm{L}}$) skew the computed means to have magnitudes that are smaller than their actual values.
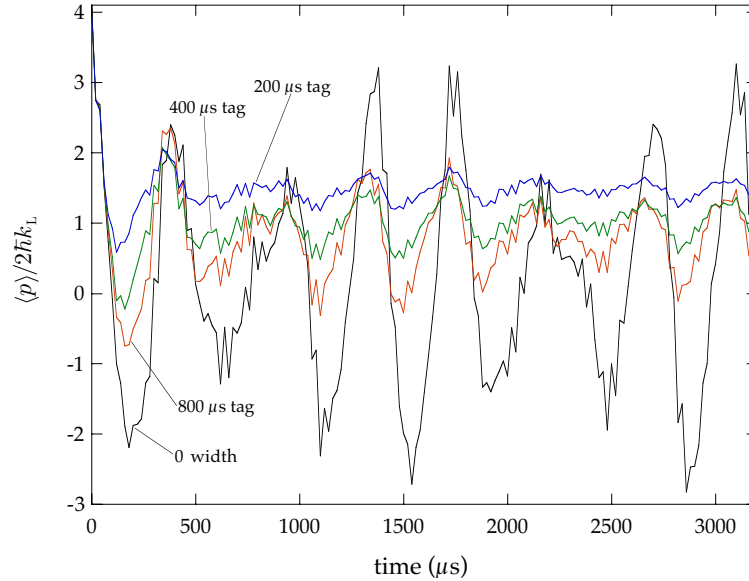

Figure 6.10: Simulation of the effects of the Raman tag width on the tunneling signal ($\alpha = 10.5$, $\bar{k} = 2.077$). The average momentum $\langle p \rangle$ is plotted every 20 μs modulation period for a single, minimum-uncertainty wave packet with an overall Gaussian envelope (out of which the Raman-selected slices are taken) centered at $(x_0, p_0) = (0, 4.1 \cdot 2\hbar k_{\mathrm{L}})$, with $\sigma_p = 1.1 \cdot 2\hbar k_{\mathrm{L}}$, to model the experimental conditions in Fig. 6.7. This calculation assumes idealized (square) π-pulse lineshapes, as in Eq. (5.26), for the Raman pulse durations used in the experiment. The case of an arbitrarily narrow velocity selection is also shown, which maximizes the tunneling-oscillation amplitude.

6.3.3   Tunneling Dependence on Wave-Packet Location

To argue that the observed tunneling was indeed between islands of stability, it was impor-
tant to demonstrate that the tunneling is sensitive to the location of the wave packet in phase
space. Just after the state preparation sequence for the above experiments, the wave packet was
moving. Thus, it was possible to displace the initial wave packet in the x-direction in phase
space simply by inserting a time delay between the usual state-preparation procedure and the
amplitude-modulated lattice phase of the experiment. Doing so produced a shift of the wave-
packet center, where the distance was proportional to the time delay, along with a shear of the
profile of the wave packet due to dispersion effects. Fig. 6.11 shows the usual zero-delay case
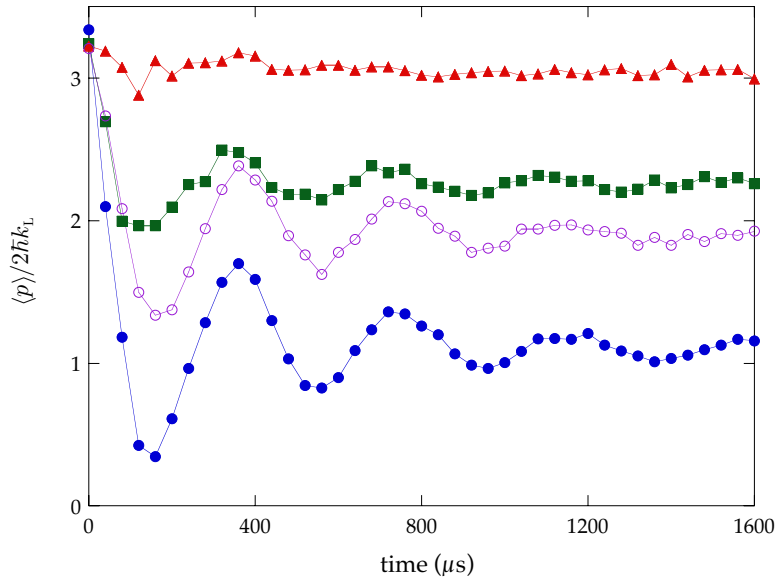compared to data with three different time delays, corresponding to displacements of $1/4$, $1/2$,

Figure 6.11: Comparison of chaos-assisted tunneling ($\alpha = 10.5$, $\hbar = 2.08$) for different free-
drift times before the standing-wave interaction, which amount to different displacements of
the initial condition in the x-direction in phase space, as illustrated in Fig. 6.12. The strongest
oscillations occur for zero drift time (filled circles), where the initial wave packet is centered
on the island of stability as in Fig. 6.4. The oscillations are significantly suppressed for a 3.8
μs drift time (squares), which displaces the initial wave packet center by $1/4$ of a period of
the standing wave. Tunneling oscillations are completely suppressed for a 7.6 μs drift time
(triangles), corresponding to a $1/2$-period offset of the initial wave packet. For a 15.1 μs drift
time (open circles), the wave packet is again centered on the island, and coherent oscillations
are restored. The data here were averaged over 20 iterations of the experiment.

and 1 full period of the lattice potential. Schematic plots of the initial conditions in the classical phase space are shown in Fig. 6.12 for these four cases. The tunneling oscillations are strongest for zero time delay, when the wave packet was centered on the island. For the 1/4-period displacement, the wave packet was centered in the chaotic region next to the island, and the tunneling oscillations are significantly suppressed. For the 1/2-period displacement, the wave packet was centered in the outer stability region, and the tunneling oscillations are almost completely suppressed. For the longest time delay, the wave packet was displaced by a full period of the potential and thus is again centered on the island. The tunneling oscillations return
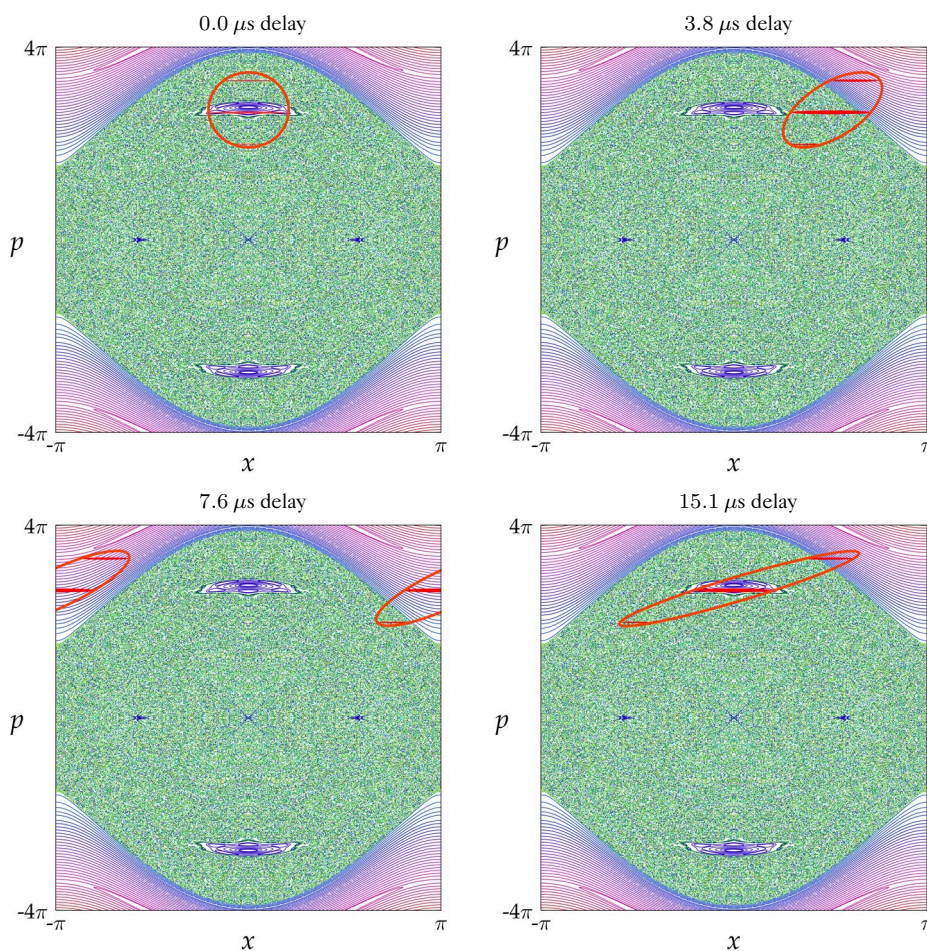

Figure 6.12: Initial conditions in phase space for the four time delays used in obtaining the data of Fig. 6.11. The large ellipse around the three narrow population slices in each case marks the overall profile of the wave packet to guide the eye.

in this case, but with smaller amplitude due to the stretched character of the wave packet after the dispersive free evolution. Hence, it is clear that the islands of stability were important in supporting the tunneling in this experiment.

We have also displaced the center of the wave packet in the p-direction in phase space by changing the amplitude of the lattice phase shift during the state preparation (and adjusting the subsequent evolution period in the lattice accordingly). For the experimental parameters here, we varied the wave packet center in steps of $0.5 \cdot 2\hbar k_{\mathrm{L}}$, and we observed strong tunneling when the wave packet was centered at $p/2\hbar k_{\mathrm{L}} = 3$, 3.5, and 4, while tunneling was suppressed at the other values outside this range.

6.4   Chaos-Assisted Tunneling

In considering the tunneling phenomenon in the experiment, we have thus far focused only on the role of the islands of stability in the tunneling. However, as we will now discuss, the chaotic region surrounding the islands is important in enhancing the tunneling process, and we will argue that the tunneling in the experiment is due to *chaos-assisted tunneling*.

The possibility of tunneling enhancement by classical chaos was first introduced in a numerical study by Lin and Ballentine [Lin90], where it was found that the tunneling rate between islands of stability in the periodically driven, double-well potential could be orders of magnitude larger than the tunneling rate in the undriven (integrable) double well. While the presence of two islands related by a discrete symmetry is important in supporting the tunneling in this system [Peres91a], the authors attributed the increased tunneling rate to the presence of the chaotic region in the classical phase space. It was subsequently shown that the tunneling rate is correlated with the degree of overlap of the tunneling states with the chaotic region [Utermann94], which also points to the role of the chaotic sea as a catalyst for the tunneling. This enhancement of the tunneling was understood in [Bohigas93; Tomsovic94] (where the term "chaos-assisted tunneling" was introduced) in terms of an avoided crossing of the tunneling doublet with a third level associated with the chaotic region, which can greatly increase the tunnel splitting. Because the (quasi)energies of the chaotic states exhibit strong and irregular

dependence of the system parameters, the tunneling rate also exhibits irregular fluctuations over orders of magnitude [Roncaglia94; Zanardi95; Mouchet01], sometimes reaching zero for exact crossings of the tunneling doublet (the "coherent destruction of tunneling" [Grossman91]). The smooth, universal dependence of the tunneling rate on $\hbar$, as mentioned above for the double-well tunneling, is therefore lost for chaos-assisted tunneling. In addition to this three-state picture, chaos-assisted tunneling has also been understood in terms of the dominance of indirect paths, which are multi-step paths that traverse the chaotic region, over direct paths, which tunnel in a single step and are responsible for regular (two-state) tunneling [Frischat98]. Thus, chaos-assisted tunneling occurs as small portions of the population from the initial wave packet break off, transport through the chaotic region, and then accumulate in the symmetric region, without a large population building up in the chaotic region [Tomsovic94; Tomsovic01]. By contrast, direct tunneling occurs with an always negligible population in the intermediate region.

The sense in which we mean "chaos-assisted tunneling" here is the influence of the chaotic region on tunneling transport between symmetry-related regions in phase space, but this term has also been applied in the sense of open systems, where the tunneling implies an escape from a bound state. In this vein, chaos-assisted tunneling has been invoked to explain fluctuations in the energy and rate of ionization of Rydberg atoms in microwave fields [Zakrzewski98], and also to explain mode lifetimes in weakly deformed optical micro-resonators [Nöckel97].

Previous experimental work in chaos-assisted tunneling has been performed in the spectroscopy of a microwave resonator in the shape of an annular billiard [Dembowski00]. The authors measured the dependence of the quasidoublet splittings on the locations of the states in phase space and on the eccentricity of the cavity, demonstrating an enhancement in the splitting for states near the border between the stable and chaotic regions. Chaos-assisted tunneling has also been invoked to explain features in the decay of superdeformed nuclear states to normal-deformed states [Åberg99], although the interpretation here is not entirely straightforward [Tomsovic01]. It is also worth noting that another atom-optics experiment studies tunneling of atoms in an optical lattice of double wells [Haycock00], where the classical description is chaotic as a result of the coupling of the center-of-mass motion to the spin state of the atom

[Ghose01]. So far, though, the symptoms of chaos-assisted tunneling that we describe below have not been observed in this system. Other experiments [Fromhold94; Wilkinson96a] consider the transport in the resonant tunneling diode, where a strong magnetic field induces chaos in the classical limit. However, the tunneling here is enhanced by energy resonances of states on either side of a barrier (corresponding to periodic orbits in the chaotic quantum-well region), and thus the tunneling is not enhanced by the chaos in the sense of this chapter.

6.4.1 Singlet-Doublet Crossings

We will now review the simplified three-state model introduced in [Bohigas93; Tomsovic94] because of its importance in understanding chaos-assisted tunneling and its utility in interpreting the experimental data. Because we are considering a periodically driven system, though, we will consider a Floquet-Hamiltonian model as in [Kohler98], rather than the original Hamiltonian model. We recall from Section 4.5.1 that the Floquet states are eigenstates of the unitary evolution operator $U(t+1, t)$ over one period of the modulation, with eigenvalue $\exp(-i\epsilon_n/\hbar)$, where ϵ_n is the quasienergy. The eigenstates can also be written as

$$|\psi_n(t)\rangle = e^{-i\epsilon_n t/\hbar}|\chi_n(t)\rangle \ , \tag{6.13}$$

where the state $|\chi_n(t)\rangle$ is periodic in time with the same period as the modulation. Thus, the quasienergies represent the phase evolution of the Floquet states (in a stroboscopic sense), just as the energies govern the phase evolution of the energy eigenstates for autonomous systems. The periodic states $|\chi_n(t)\rangle$ are also eigenstates of the Floquet Hamiltonian [Mouchet01],

$$\mathcal{H} := H - i\hbar\partial_t, \tag{6.14}$$

with eigenvalue ϵ_n. We will therefore construct a model Floquet Hamiltonian that captures the essence of chaos-assisted tunneling.

We consider a doublet of tunneling states, localized on the two islands of stability (regular regions), with quasienergies ϵ_r and $\epsilon_r + \delta_r$, so that δ_r parameterizes the tunneling rate in the absence of interaction with other levels. These states have opposite parity, and for the sake

of concreteness, we can take the state with quasienergy ϵ_r to be of even parity. We also consider a third state in the chaotic region (although we note that three-level crossings can also be induced by states in other stable regions [Bonci98; Frischat98; Brodier01]), with quasienergy $\epsilon_r + \Delta_c$. Without loss of generality we may assume that this state has even parity; notice that the states in the chaotic region do not generally occur in narrowly spaced doublets, so that we can ignore the effect of the corresponding state of odd parity. The chaotic state does not interact with the odd member of the tunneling doublet, but we assume that there is some nonzero interaction between the two even states. We may then write the model Floquet Hamiltonian as [Bohigas93; Tomsovic94; Kohler98]

$$\mathcal{H} = \begin{pmatrix} \epsilon_r + \delta_r & 0 & 0 \\ 0 & \epsilon_r & \beta/2 \\ 0 & \beta/2 & \epsilon_r + \Delta_c \end{pmatrix} \, , \tag{6.15}$$

where β represents the coupling between the chaotic state and the even regular state. Thus, the two coupled states undergo an avoided crossing, with quasienergy solutions of the same form as
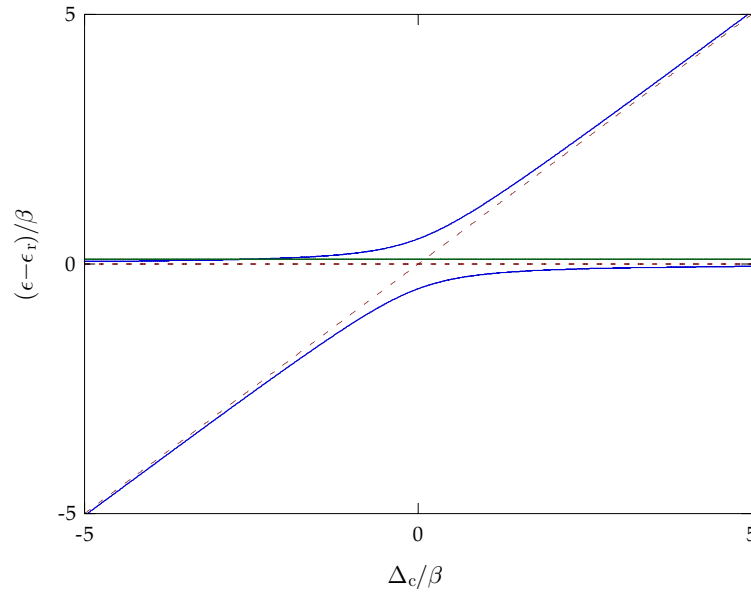

Figure 6.13: Illustration of a three-level avoided crossing of a tunneling doublet with a third (chaotic) state, as described by the model (6.15). The behavior of the three quasienergies is shown as a function of the detuning Δ_c of the chaotic state, for an unperturbed doublet splitting $\delta_r/\beta = 0.1$. The chaotic state interacts with the regular state of the same parity (both shown as blue lines), and the other tunneling state (the green line) is unaffected by the crossing in this simple model. The dashed lines show the two repelling states in the absence of any coupling.

in the two-level case in Eqs. (6.5)-(6.8), while the odd regular state remains unchanged. This behavior is illustrated in Fig. 6.13. In the case where the coupling energy $\beta/2$ is large compared to the two-level splitting δ_{r} (which is the case when the regular states have substantial overlap with the surrounding chaotic region), the tunnel splitting can be greatly enhanced, becoming of the order of $\beta/2$ between the odd state and either of the even states near the center of the crossing. As one might expect in an avoided crossing, the even regular state and the chaotic state exchange their character as Δ_{c} is swept through zero, as verified numerically in [Latka94b]. Thus, near the center of the crossing, the two even states each have population both in the islands and in the chaotic region, whereas away from the crossing it is possible to clearly distinguish a predominantly regular and predominantly chaotic even state. In a singet-doublet crossing, one expects a complicated time dependence, compared to the sinusoidal two-state tunneling, because three states will be excited by a wave packet localized on a single island. In general, the three splittings will all be different, leading to complicated beating in the time domain [Kohler98].

6.4.2   Comparison with Integrable Tunneling

The tunneling that we have studied is between two oppositely directed modes of motion. In unmodulated optical lattices, however, Bragg scattering is a well-known dynamical-tunneling mechanism, as we discussed in Section 2.7.1. Bragg scattering produces similar results to the tunneling that we have described, including sensitivity to the same broken symmetry that we discussed above, even though there is no classical chaos without a modulation of the lattice. It was therefore important to demonstrate that the tunneling here is not simply Bragg scattering, but that the amplitude modulation has a substantial effect on the tunneling dynamics. We have done this already to a certain extent by demonstrating that the initial state must be centered on the island of stability for tunneling to occur (Bragg scattering occurs between plane-wave states, which are delocalized in position, and thus should not be sensitive to spatial displacements of the initial condition). However, a direct comparison between tunneling in chaotic and integrable systems is also illuminating.

A sensible integrable counterpart of the modulated system arises by using the optical

lattice with constant amplitude, where the potential depth is taken to be V_0. Doing so produces a pendulum, such that the lattice intensity is the same, on average, as in the amplitude-modulated system. The phase space for the pendulum corresponding to the experimental conditions in Fig. 6.4 is shown in Fig. 6.14, along with the same initial condition as before. The wave packet is centered outside the separatrix, so that classical transport to the opposite momentum region is also forbidden here. However, high-order Bragg scattering, which is a manifestation of quantum above-barrier reflection [Heller99], allows quantum oscillatory transport between these momentum regions.
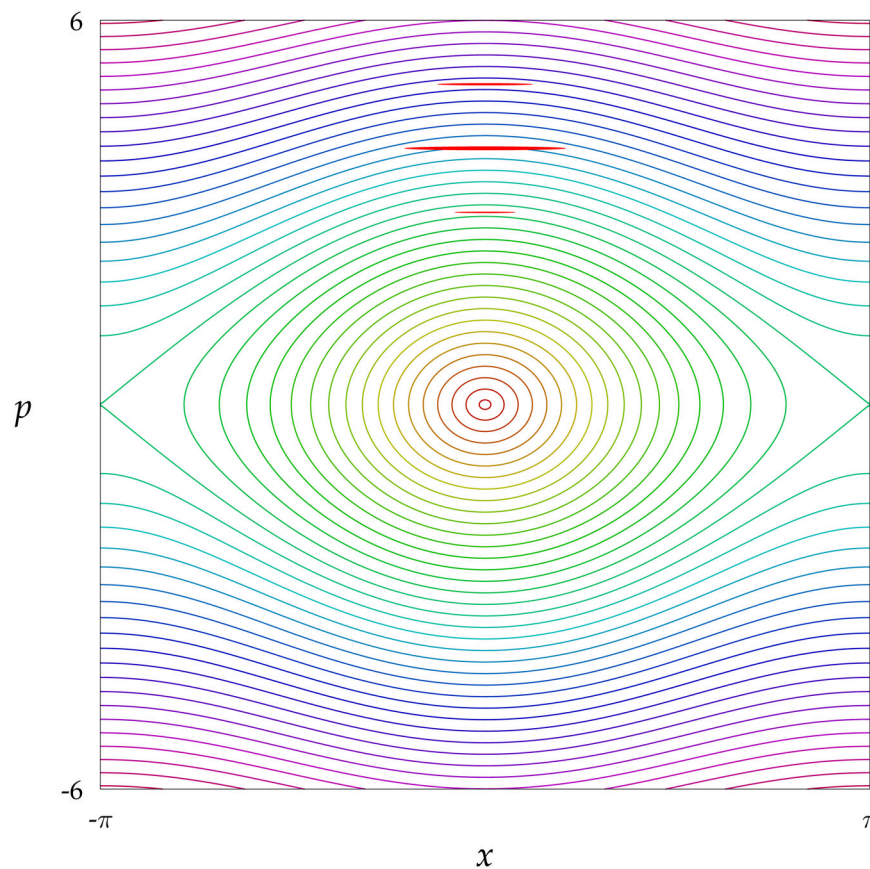

Figure 6.14: Phase space of the pendulum, with the same average potential amplitude as the modulated-pendulum case in Fig. 6.4. The same initial condition is also shown here. The initial state is centered outside the separatrix, so that classical transport to the opposite (symmetric) momentum region is also forbidden here. Notice that the momentum axis is in pendulum scaled units (i.e., multiples of $2\hbar k_{\mathrm{L}}$), rather than the scaled units for the modulated pendulum.

We recall from Section 2.7.1 that the Bragg oscillation frequency is

$$\Omega'_{\text{B},n} = \frac{\alpha^n}{\bar{k}^{2n-1}[(n-1)!]^2} \ ,$$
(6.16)

when adapted to the scaled units of the amplitude-modulated pendulum. In this form, it is not obvious that Bragg scattering has the expected universal dependence $\exp(-S/\bar{k})$ for two-state tunneling that we mentioned above. Since tunneling occurs from some initial momentum $(n/2)\bar{k}$ to $-(n/2)\bar{k}$ (for integer n) as an nth-order scattering process, the order n is effectively a function of $\bar{k}$. Then, in the semiclassical limit of large n, we can invoke Stirling's approximation, and the Bragg rate becomes

$$\Omega'_{\text{B},n} \simeq \frac{1}{2\pi} \left[\frac{(2p)^2}{\alpha e^2} \right]^{-p/\bar{k}} ,$$
(6.17)

which is consistent with the expected scaling with $\bar{k}$. Notice that the factor in the square braces is greater than unity, since to be in the Bragg regime (where population in the intermediate
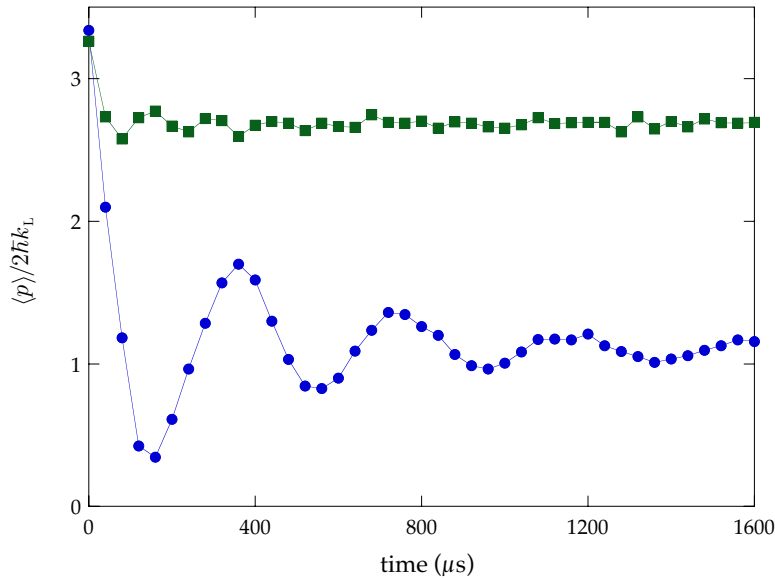

Figure 6.15: Comparison of chaos-assisted tunneling oscillations (circles) to transport in the corresponding quantum pendulum (squares). The experimental conditions are $\alpha = 10.5$ and $\bar{k} = 2.08$ in the modulated case, with the same average intensity used in the pendulum case. No tunneling oscillations are observed in the pendulum case over the interaction times studied in the experiment. The expected period for 8th-order Bragg scattering is 1 s, which is much longer than the 400 μs period of the tunneling between islands of stability. The data here were averaged over 20 iterations of the experiment.

states can be adiabatically eliminated) the wave packet must be outside the classical pendulum separatrix, which implies that $|p| > 2\sqrt{\alpha}$.

The tunneling oscillations of Fig. 6.5 are compared with the behavior of the corresponding pendulum in Fig. 6.15. No tunneling oscillations are visible in the integrable case over the time scale studied in the experiment. Since the initial distribution is peaked near $4 \cdot 2\hbar k_{\mathrm{L}}$, the dominant transport process in the pendulum is 8th-order Bragg scattering. For $n = 8$, $\alpha = 10.5$, and $\bar{k} = 2.08$, the Bragg period is about 1 s, which is much longer than the $400~\mu s$ period of the tunneling oscillations in the chaotic case (and thus the experimental Bragg measurement is in accord with our expectations).

We have also demonstrated tunneling in a parameter regime that is closer to the classical limit ($\bar{k} = 1.04$), as shown in Fig. 6.16. The initial distribution here is peaked around $8 \cdot 2\hbar k_{\mathrm{L}}$, and so this coherent, 32-photon process is similar to 16th-order Bragg scattering. The expected Bragg period here is 20 years, which is long compared to the $250~\mu s$ period of the tunneling in

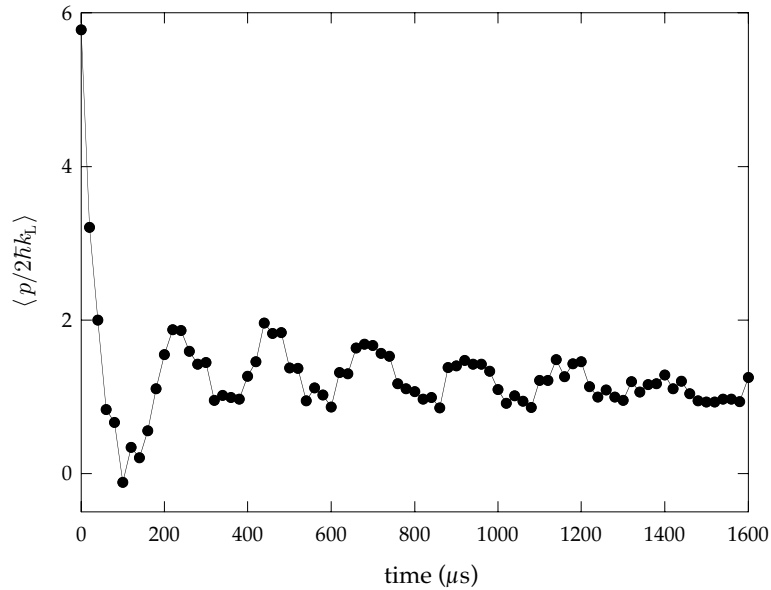Figure 6.16: Tunneling oscillations for $\alpha = 11.2$, $\bar{k} = 1.04$ ($10~\mu s$ modulation period). The corresponding two-state (integrable) tunneling mechanism is 16th-order Bragg scattering, which has an expected period of 20 years. The observed tunneling rate is clearly much smaller than the expected Bragg period. The data here were averaged over 10 iterations of the experiment.

the chaotic case, and is even long compared to the coherence time of a graduate student. Thus, it is clear that in some sense the chaos enhances the transport, in that the tunnel splittings are much larger in the chaotic case than in the corresponding integrable case.

Of course, it could be the case that the amplitude modulation enhances the two-level tunneling rate without the influence of a third, chaotic state, especially in view of the rapid dependence of the Bragg splitting on the lattice intensity. Although we provide additional experimental evidence for chaos-assisted tunneling below, we will now derive a simple estimate for the direct tunneling rate with the modulation. Since Bragg scattering represents the two-level transport mechanism in this system, and corresponds to a resonantly coupled two-level system if the proper momentum symmetry condition is satisfied, we can use the well-established solution to the two-level atom (without damping) exposed to a resonant driving field with time-dependent intensity [Allen87]. In this case we define the pulse integral,

$$\phi = \int_0^t \Omega_{\mathrm{B},n}(t')\, dt' \;\;,$$ (6.18)

in terms of which the tunneled population can be written as $\sin^2(\phi/2)$ (note that $\phi = \Omega_{\mathrm{B},n}t$ for constant drive, as in normal Bragg scattering). Since the tunneling period is substantially longer than the modulation period, we can simply average the Bragg rate over a modulation period, and thus the modulation enhances the two-level tunneling rate by a factor

$$\int_0^1 [2\cos^2(\pi t)]^n \, dt$$ (6.19)

for nth-order transport. This factor is about 50 for the $\mathchar'26\mkern-9mu k = 2.08$ case and about 9000 for the $\mathchar'26\mkern-9mu k = 1.04$ case. Neither of these numerical values is sufficiently large to explain the enormous differences in the tunneling rates in the integrable and chaotic cases.

6.4.3   Tunneling Dependence on Parameter Variations

To establish that the tunneling in the modulated lattice is chaos-assisted tunneling, it is also important to examine the dependence of the tunneling as the two experimental parameters (α and $\mathchar'26\mkern-9mu k$) are varied. As we noted above, the dependence of the tunneling rate should be very different for direct and chaos-assisted tunneling. In this section, we examine the variation of

the tunneling as a function of α for two different values of $\hbar$. Operationally, α is a much more convenient parameter to vary, because it only requires a change in laser intensity, whereas $\hbar$ is more difficult because it requires changing both the laser intensity and the modulation period (to keep α fixed) as well as a new set of parameters for the SPASM state preparation (to maintain the initial condition at the same phase-space location). While we do not necessarily expect
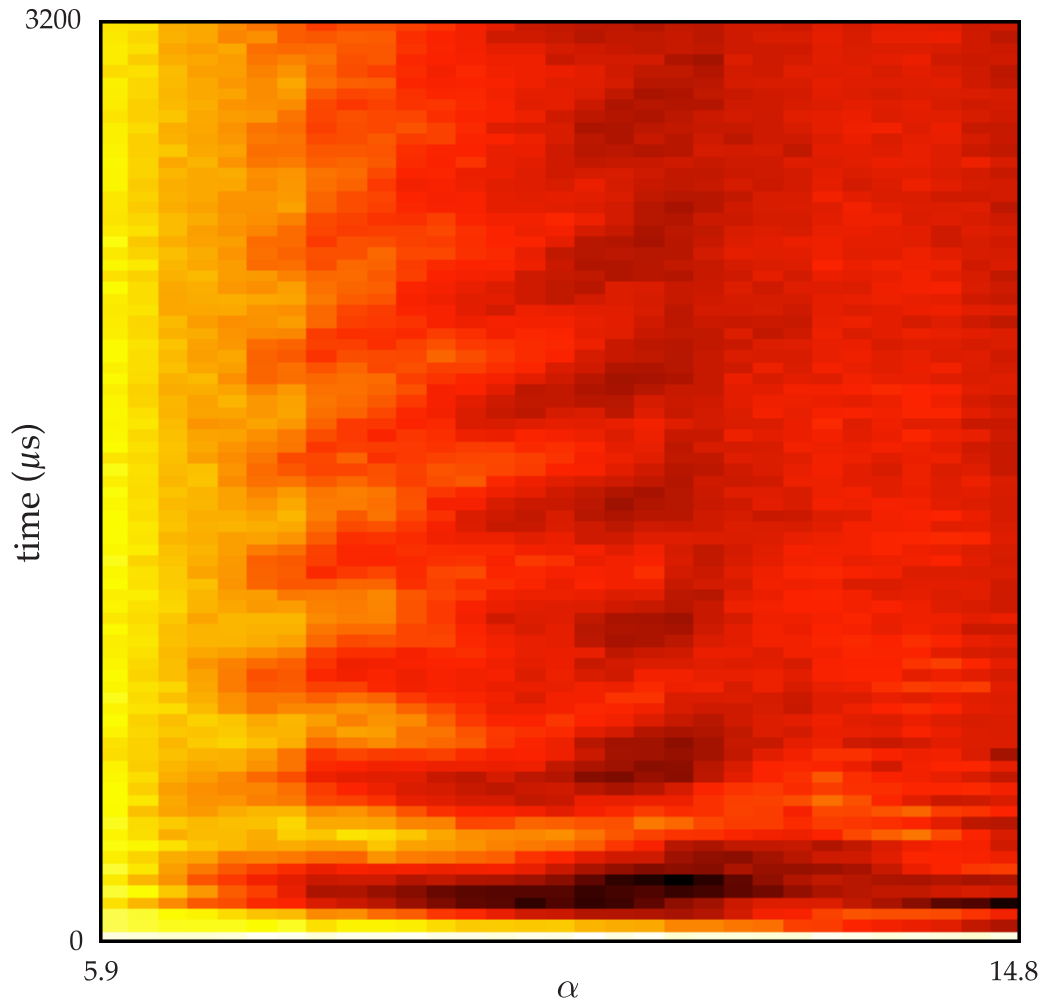

Figure 6.17: Dependence of the tunneling as the optical-lattice intensity α is varied for $\hbar = 2.08$ (20 μs modulation period). The color indicates the value of $\langle p \rangle$, with black representing the most negative values and white the most positive. The tunneling is absent at the extreme values of α shown here, but tunneling oscillations appear in the center of the α range. This behavior is consistent with the avoided-crossing mechanism for chaos-assisted tunneling. The data here were averaged over 10 iterations of the experiment.

to see rapid variations in the tunneling rate as we vary α, due to inhomogeneous broadening (different atoms see different optical intensities, depending on their transverse location in the optical lattice, leading to about a 5% spread in α over the atomic sample), there are nevertheless signatures of three-state tunneling in the data.

The dependence of the tunneling oscillations in the measured evolution of $\langle p(t) \rangle$ is shown in Fig. 6.17 for $\bar{k} = 2.08$. Tunneling is visible in the range of α from about 7 to 14, but is suppressed outside this range. Below this range the tunneling is presumably too slow to be observed (see the Floquet-spectrum analysis in the next section), and above this range the outer islands have completely dissolved into the chaotic sea, so that we no longer expect clean tunneling to occur. The tunneling rates for this data are plotted in Fig. 6.18. The tunneling rate does not fluctuate strongly as α changes, but there are two interesting features to notice. The first is that the tunneling rate *decreases* as a function of α. This dependence is the opposite of our expectation of direct tunneling, where as we have seen above the tunneling rate should
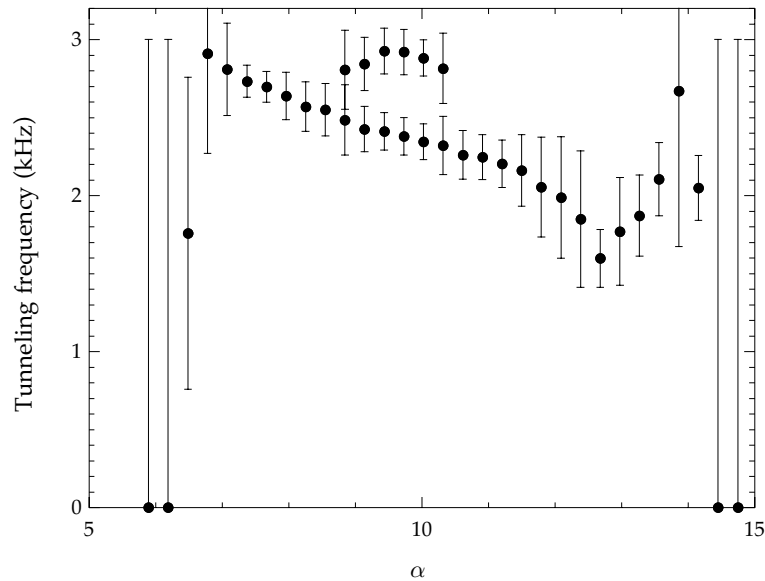

Figure 6.18: Dependence of the tunneling rate on the well depth α, for $\bar{k} = 2.08$ (20 μs modulation period). The periods were extracted from the data in Fig. 6.17 using both numerical Fourier transform and nonlinear fitting techniques. The error bars account for both fitting uncertainty and the width of the spectral peaks. In the range of α from 8.9 to 10.3, two distinct frequencies can be resolved in the tunneling data. The zero-frequency data points at the edges of the plot indicate that no tunneling frequency could be extracted from the data at these locations.
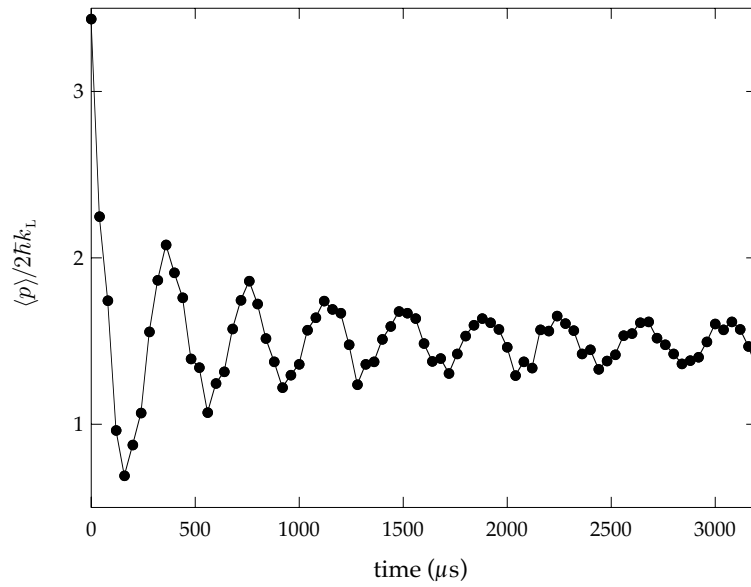
Figure 6.19: Example of tunneling oscillations from Fig. 6.17, where a single tunneling frequency persists for the maximum duration of the optical-lattice interaction. The parameters are $\alpha = 8.0$, $\hbar = 2.08$. The data points are connected by lines for clarity.
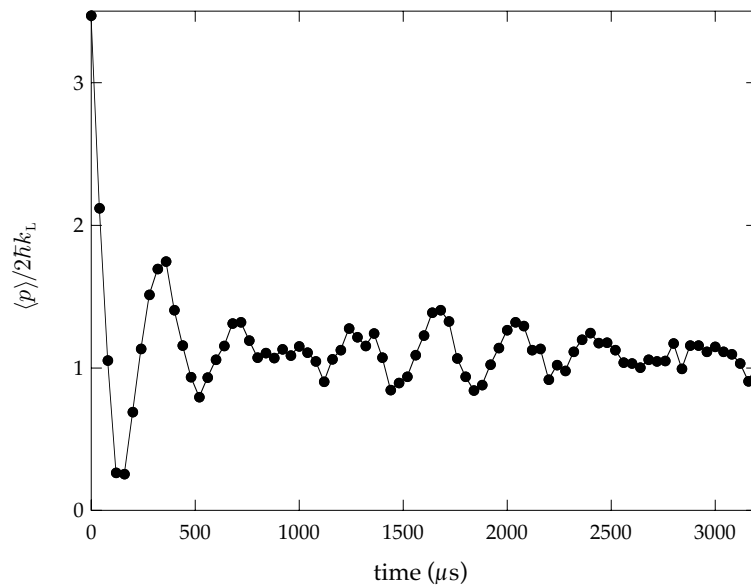

Figure 6.20: Example of tunneling oscillations from Fig. 6.17, where two tunneling frequencies are clearly present. The parameters are $\alpha = 9.7$, $\hbar = 2.08$. The data points are connected by lines for clarity.

increase with α, following a power-law dependence. This behavior is thus strong evidence that the tunneling is chaos-assisted, where one or more chaotic levels has a definite influence on the doublet splitting. The second feature to notice is that two frequencies are clearly resolvable in the tunneling in a comparatively narrow window in α (from about 8.5 to 10.5). The one- and two-frequency behaviors of the tunneling are illustrated in Fig. 6.19, where one tunneling frequency is evident (for $\alpha = 8.0$), and in Fig. 6.20, where the beating of two frequencies is clearly
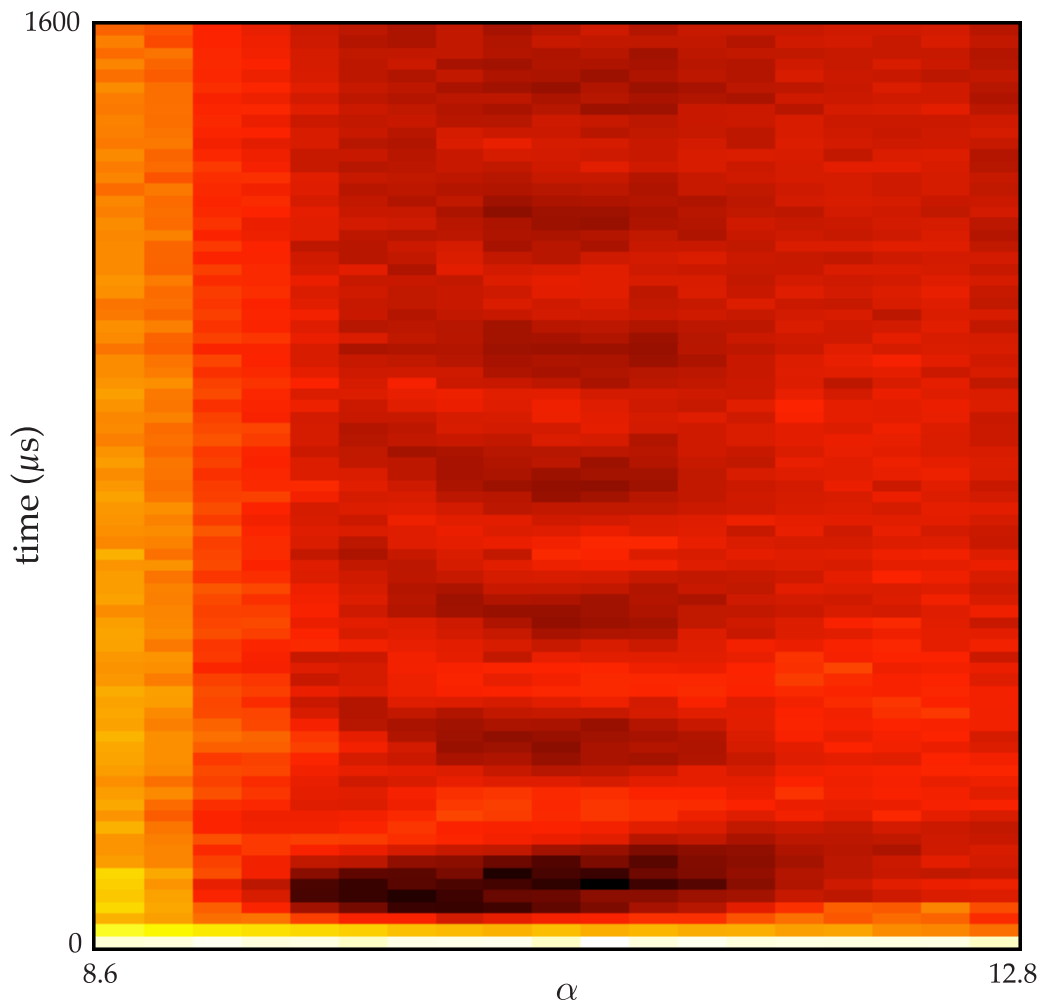

Figure 6.21: Dependence of the tunneling as the optical-lattice intensity α is varied for $k = 1.04$ (10 μs modulation period). The color indicates the value of $\langle p \rangle$. The behavior here is qualitatively similar to the behavior in Fig. 6.17, but the tunneling occurs in a substantially narrower interval in α. The data were averaged over 10 iterations of the experiment.

apparent (for $\alpha = 9.7$). Thus, there is some sensitivity of the tunneling to variations in α in this regime. This behavior is also consistent with the three-state model near the center of a singlet-doublet crossing. In this model, the initial wave packet populates a regular state (localized on the islands) and two hybrid states, which have population in both the islands and in the chaotic sea. There should thus be two frequencies associated with the tunneling, corresponding to the two splittings between the regular state and the two hybrid states. In general, these two splittings will not be equal, but should be similar near the center of the avoided crossing, leading to two-frequency beating in the tunneling dynamics.

The variation of the tunneling behavior in the $\bar{k} = 1.04$ case is plotted in Fig. 6.21, with the extracted tunneling rates plotted in Fig. 6.22. The observed tunneling rates appear to have weaker dependence on α than in the $\bar{k} = 2.08$ case. However, the tunneling is only visible in a much narrower interval in α, from about 9.5 to 12.5. Thus, in a sense, the tunneling here is more sensitive to variation in α than in the $\bar{k} = 2.08$ case.
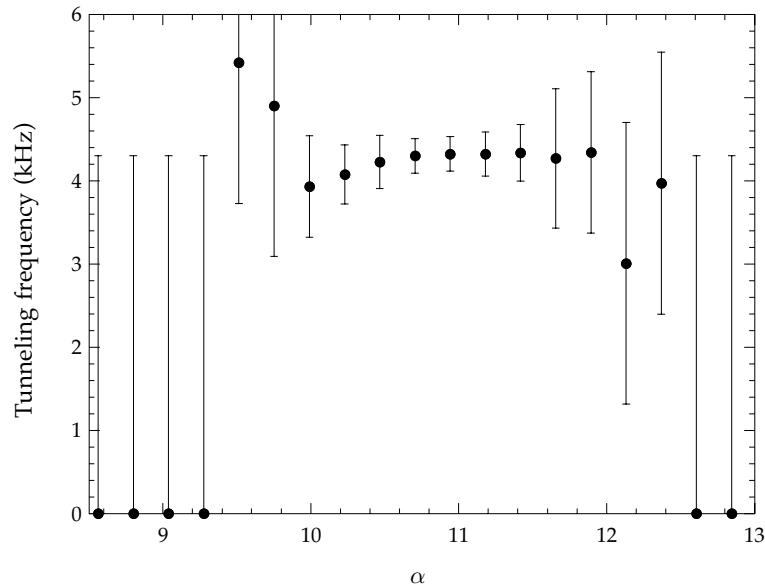

Figure 6.22: Dependence of the tunneling rate on the well depth α, for $\bar{k} = 1.04$ (10 μs modulation period). The periods were extracted from the data in Fig. 6.21 using both numerical Fourier transform and nonlinear fitting techniques. The error bars account for both fitting uncertainty and the width of the spectral peaks. The zero-frequency data points at the edges of the plot indicate that no tunneling frequency could be extracted from the data at these locations.

One question that remains is why the tunneling rate does not go smoothly to zero at the edges of the α intervals where tunneling is observed, especially at the lower end of the interval where the tunnel splitting is expected to become very small. In the experiment, the disappearance of the tunneling as α is swept comes about as the oscillations decrease in amplitude and become damped more quickly, until the oscillations are no longer discernible. One possible explanation is the change in the location of the two islands, which move to larger momentum as α increases (see the next section for an empirical expression for the island locations). In the experiment, the initial condition was held fixed as α is swept, so that there may have been less overlap with the tunneling Floquet states if the islands moved too far. However, over the intervals where tunneling was observed, the islands moved only by $\pm 0.3 \cdot 2\hbar k_{\mathrm{L}}$ for both the $\bar{k} = 2.08$ and the $\bar{k} = 1.04$ data sets, which is a substantially smaller amount than the respective $\sigma_p = 1.7 \cdot 2\hbar k_{\mathrm{L}}$ and $\sigma_p = 2.1 \cdot 2\hbar k_{\mathrm{L}}$ momentum uncertainties of the initial conditions in the two cases. Thus, misalignment of the initial conditions does not account for the disappearance of the tunneling at the extreme α values here. Another possible explanation lies in a suggestion by [Latka94a] that three-level tunneling is more robust to a symmetry-breaking interaction than two-level tunneling. Since the range of populated quasimomenta (and thus the degree of broken symmetry) is fixed by the Raman velocity selection, the tunneling away from the avoided crossings may simply disappear, as opposed to being manifested as a slow tunneling oscillation.

6.4.4   Floquet Spectra

In the context of understanding the observed tunneling dependence on α, it is useful to consider the quasienergy spectrum for this system. Computed spectra for the $\bar{k} = 2.077$ and $\bar{k} = 1.039$ cases are plotted in Figs. 6.23 and 6.24, respectively. These spectra only show the states with definite parity, falling on the symmetric ladder of momentum states $p = n\bar{k}$ (for integer n), corresponding to zero quasimomentum. The quasienergies were calculated by numerically constructing the unitary evolution operator for one period of the modulation and then diagonalizing the resulting operator. The even and odd tunneling states are also highlighted in these spectra. These states were identified by finding the states with maximum overlap with a minimum-uncertainty Gaussian wave packet that was centered on the fixed point of the island and had

the same aspect ratio as the elliptical trajectories near the fixed point (i.e., where the linearized equations of motion are valid). The centers of the outer islands are given approximately by the empirical model

$$p_0 = \pm(2\pi + 0.1988 \cdot \alpha + 0.002953 \cdot \alpha^2 - 0.0000327 \cdot \alpha^3) \tag{6.20}$$

(with $x = 0$), which is accurate at about the 0.02% level from $\alpha = 0$ to the critical value $\alpha_c \approx$ 11.54 where these islands become unstable and bifurcate into pairs of islands. The aspect ratio of the elliptic invariant surfaces near the island centers is given approximately by the empirical model

$$\frac{\Delta p}{\Delta x} = \sqrt{\alpha(\alpha - \alpha_c)(-0.0439 + 0.00151 \cdot \alpha + 0.0000170 \cdot \alpha^2)} \ , \tag{6.21}$$

which is accurate to the 1% level or better in the same range. The tunneling states are not identified for $\alpha > \alpha_c$, where it is difficult to assign states to the island remnants.

In the spectrum for $\hbar = 2.077$, the first avoided crossing (with an even-parity state of smaller quasienergy) does not occur until about $\alpha = 7$, where the splitting also first becomes significant. This behavior is consistent with the experimental data in Fig. 6.17, where tunneling oscillations are also first observed around $\alpha = 7$. Beyond this point, the two even-parity states maintain a similar distance from the odd tunneling state, and this holds true in the regime where two tunneling frequencies are visible in the data. These two even states then move back towards each other (and the odd tunneling state) as they interact with two other even states, and this behavior may explain the decreasing tunneling rate as a function of α, although it is again difficult to pinpoint the tunneling states in this regime of large α.

In the $\hbar = 1.039$ spectrum, the singlet-doublet crossings are much more apparent. There are several clear avoided crossings involving the tunneling doublet in the range shown, but it is not until the final avoided crossing before the islands become unstable that the splitting becomes large enough to observe experimentally. The experimental observation of tunneling beginning with $\alpha = 9.5$ is thus consistent with the spectrum, although another significant avoided crossing in the spectrum suggests that tunneling might also be visible in a very narrow region

around $\alpha = 8$. The experimental tunneling stops around $\alpha = 12.5$, where the spectrum has become quite complicated and the tunneling doublet can no longer be identified.

The tunneling rates from the calculated spectra here are in good agreement with the observed rates in Figs. 6.18 and 6.22. For example, the two calculated tunneling rates for $\alpha = 10$ and $\hbar = 2.08$ are 3.0 kHz and 2.3 kHz, and the calculated tunneling rate for $\alpha = 11$ and $\hbar = 1.04$ is 4.0 kHz, all of which match the observed tunneling rates reasonably well. However, it should
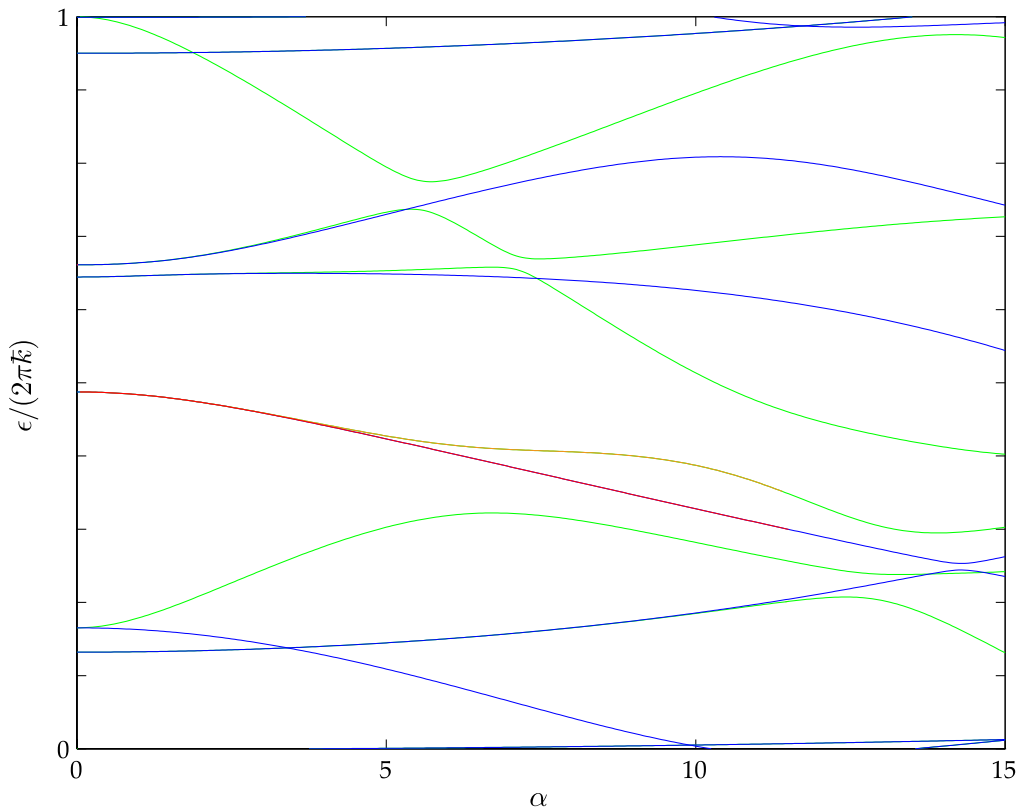

Figure 6.23: Calculated quasienergy spectrum for $\hbar = 2.077$, corresponding to a 20 μs modulation period. Quasienergies that correspond to states with large momentum (that do not interact with the states shown in this range of α) are suppressed, and the quasienergies shown are for the symmetric momentum ladder (zero quasimomentum). The quasienergies for even-parity Floquet states are shown in green, while the odd-parity states are shown in blue. The even (orange) and odd (red) states with maximal overlap with the outer stable islands are shown, up to the point where the islands bifurcate, as described in the text. The avoided-crossing behavior of the tunneling states is apparent over a broad range of α, where two chaotic states have a clear influence on the tunneling-doublet splitting.

be noted that while these spectra provide a useful basis for understanding the data, an interpretation based solely on these spectra would most likely be too simplistic to be very useful. An accurate model would at minimum need to take into account the excitation of multiple Floquet states by the initial condition, the range of quasimomenta populated after the Raman velocity selection (as we have done in Fig. 6.10), and the averaging over a range of α due to the transverse profile of the optical-lattice beam.
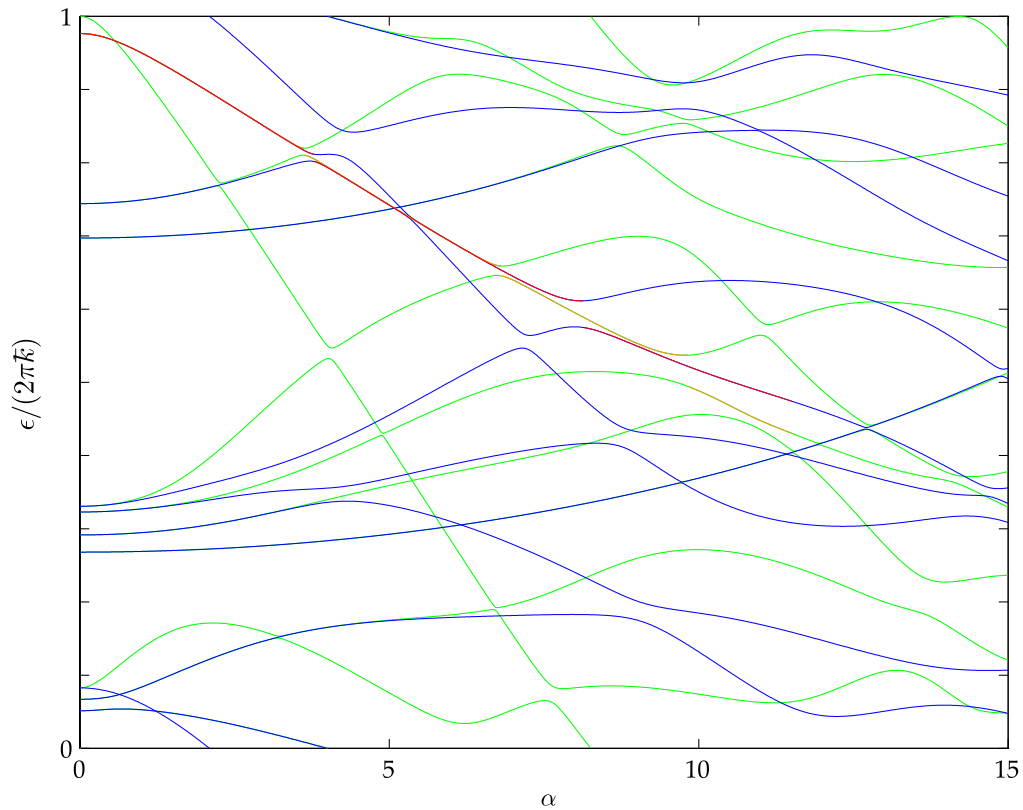

Figure 6.24: Calculated quasienergy spectrum for $\bar{k} = 1.039$, corresponding to a 10 μs modulation period. Quasienergies that correspond to states with large momentum (that do not interact with the states shown in this range of α) are suppressed, and the quasienergies shown are for the symmetric momentum ladder (zero quasimomentum). The quasienergies for even-parity Floquet states are shown in green, while the odd-parity states are shown in blue. The even (orange) and odd (red) states with maximal overlap with the outer stable islands are shown, up to the point where the islands bifurcate, as described in the text. Several avoided crossings of the tunneling doublet with chaotic states are apparent, although the splitting only becomes very large around $\alpha = 10$.

6.4.5   High Temporal Resolution Measurements

All of the data so far in this chapter have been sampled only at a particular phase of the periodic driving, corresponding to integer times in the Hamiltonian (6.11). We will now study the dynamics on a much finer time scale, which will reveal additional interesting aspects of the tunneling dynamics. Figs. 6.25 and 6.26 show the tunneling dynamics for $\bar{k} = 2.08$ (for two different values of α), and Fig. 6.27 shows the tunneling dynamics for $\bar{k} = 1.04$; in all three figures, the momentum distribution was sampled 10 times per modulation period, and the duration of the measurement covers approximately one full period of the amplitude modulation. Besides the island-tunneling process, which is visible as the slowest oscillation, there are two other oscillatory motions that are common to the three plots. The more obvious of these features appears
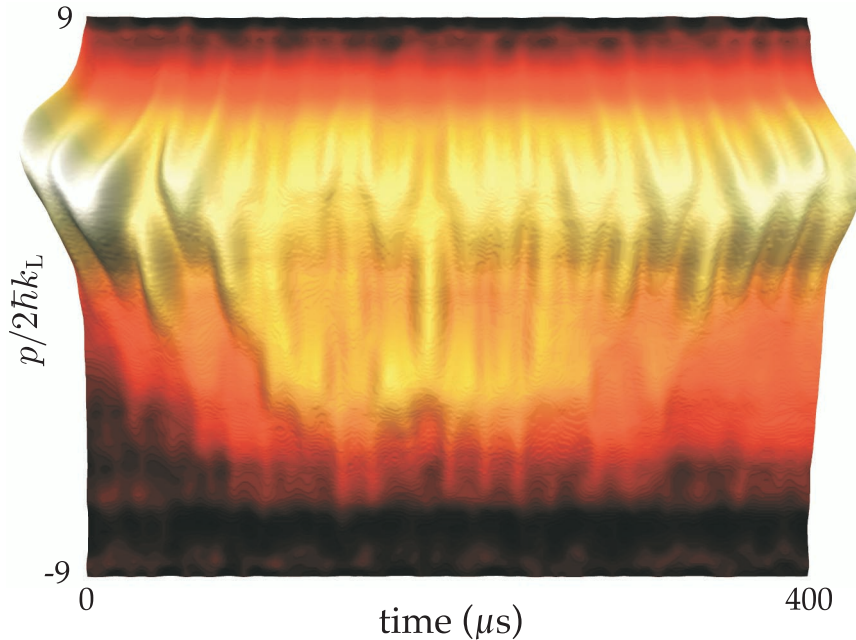

Figure 6.25: Experimental momentum-distribution evolution of chaos-assisted tunneling for $\bar{k} = 2.08$ ($T = 20\ \mu s$) and $\alpha = 7.7$. The distribution was sampled every 2 μs out to 400 μs, covering the first full tunneling oscillation. The classical oscillations (with the same period as the modulation period) are evident, as well as more complicated oscillations into the intermediate chaotic/stable region near $p = 0$. The phase space (see Appendix C) is characterized by the two (symmetry-related) tunneling islands as well as a doublet of stable islands near $p = 0$. These distributions were averaged over 10 iterations of the experiment.

as a fast oscillation of the initial peak, with the same period as the modulation of the potential. As the atoms tunnel to the other island, the tunneled peak oscillates in a complementary fashion. This motion can be understood in terms of the classical phase-space dynamics. A particular phase space for this system assumes a particular sampling phase for the dynamics; for the phase spaces in Appendix C, the sampling phase is the same as that used for the previous data in this chapter. To understand the present phenomenon, though, it is necessary to examine the phase space as the sampling phase varies, as illustrated in Fig. 6.28. Because of the periodic time dependence of the potential, the time parameter acts as a third dimension in phase space. Thus the islands of stability are "flux tubes" that confine classical trajectories in the higher-dimensional phase space [Averbukh95], and the islands that appear in the phase plots (Poincaré sections) are cross sections of the flux tubes. As time varies continuously, then, the islands move in oppo-
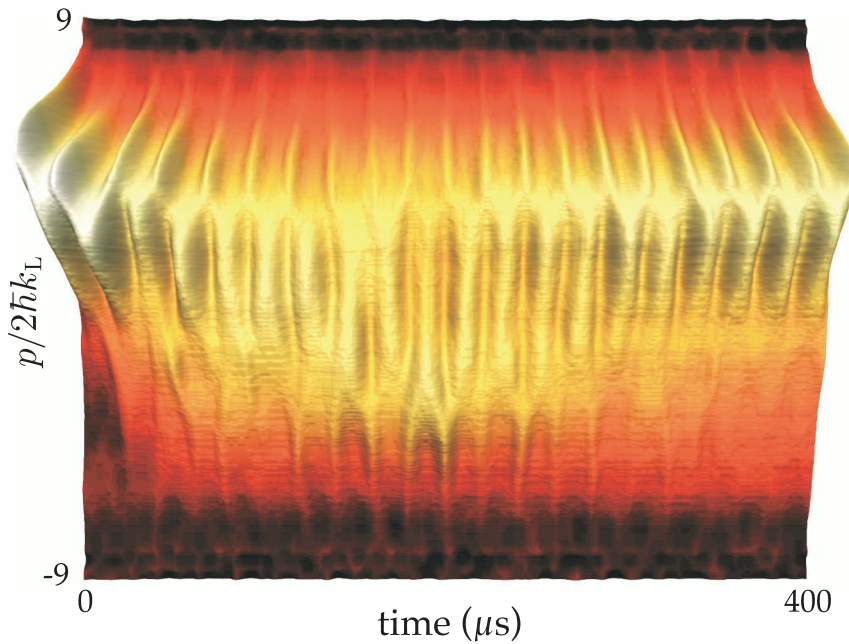

Figure 6.26: Experimental momentum-distribution evolution of chaos-assisted tunneling for $k = 2.08$ ($T = 20\,\mu$s) and $\alpha = 11.2$. The distribution was sampled every $2\,\mu$s out to $400\,\mu$s, covering the first full tunneling oscillation. The conditions are otherwise similar to those in Fig. 6.25; the oscillations in the chaotic region occur in different locations, compared to the previous case. The phase space (see Appendix C) is characterized by the two (symmetry-related) tunneling islands with only small remnants of the island near $p = 0$. These distributions were averaged over 10 iterations of the experiment.

site directions in phase space according to their mean momenta. Additionally, the islands move in the momentum direction, becoming furthest apart in momentum for integer sampling times and closest together for half-integer times. This oscillation is only significant for relatively large values of α (away from the near-integrable regime), because of the mutual repulsion of the three primary resonances in phase space. Thus, the fast oscillations of the experimental momentum distributions can be attributed to the motion of the classical phase-space islands.

The second oscillatory feature is the more relevant effect for demonstrating chaos-assisted tunneling. This oscillation is slower than the classical oscillation but also is substantially faster than the tunneling oscillation. It appears as an occasional enhancement of probability in the (predominantly) chaotic region between the two islands. This effect is particularly dramatic
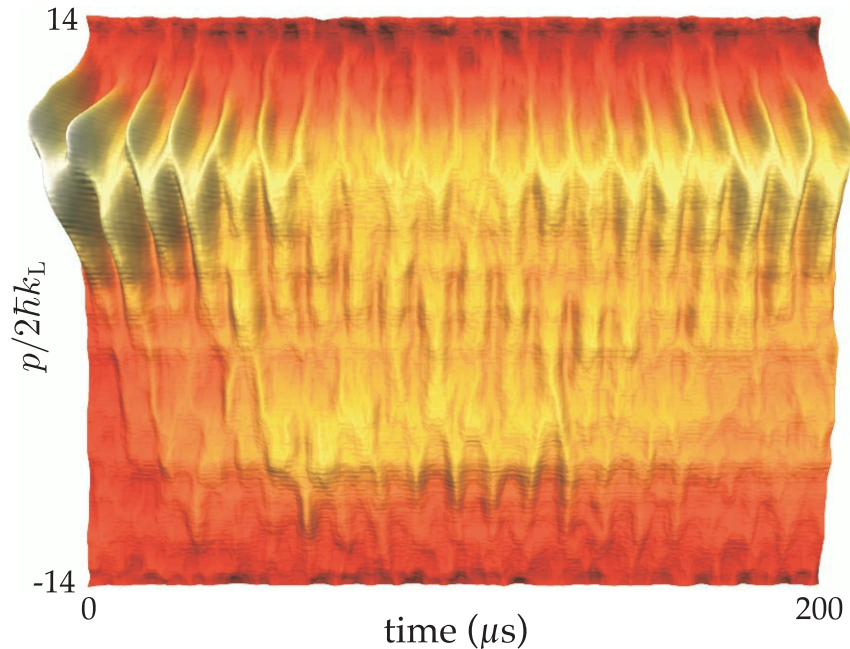

Figure 6.27: Experimental momentum-distribution evolution of chaos-assisted tunneling for $\bar{k} = 1.04$ ($T = 10$ μs) and $\alpha = 10.5$. The distribution was sampled every 1 μs out to 200 μs, covering the first full tunneling oscillation. The oscillations in the chaotic region here are more difficult to see than in Figs. 6.25 and 6.26, because of the smaller signal-to-noise ratio for these experimental conditions (the horizontal stripes are artifacts of the CCD camera). The phase space (see Appendix C) is characterized by the two (symmetry-related) tunneling islands with only small remnants of the island near $p = 0$. These distributions were averaged over 10 iterations of the experiment.
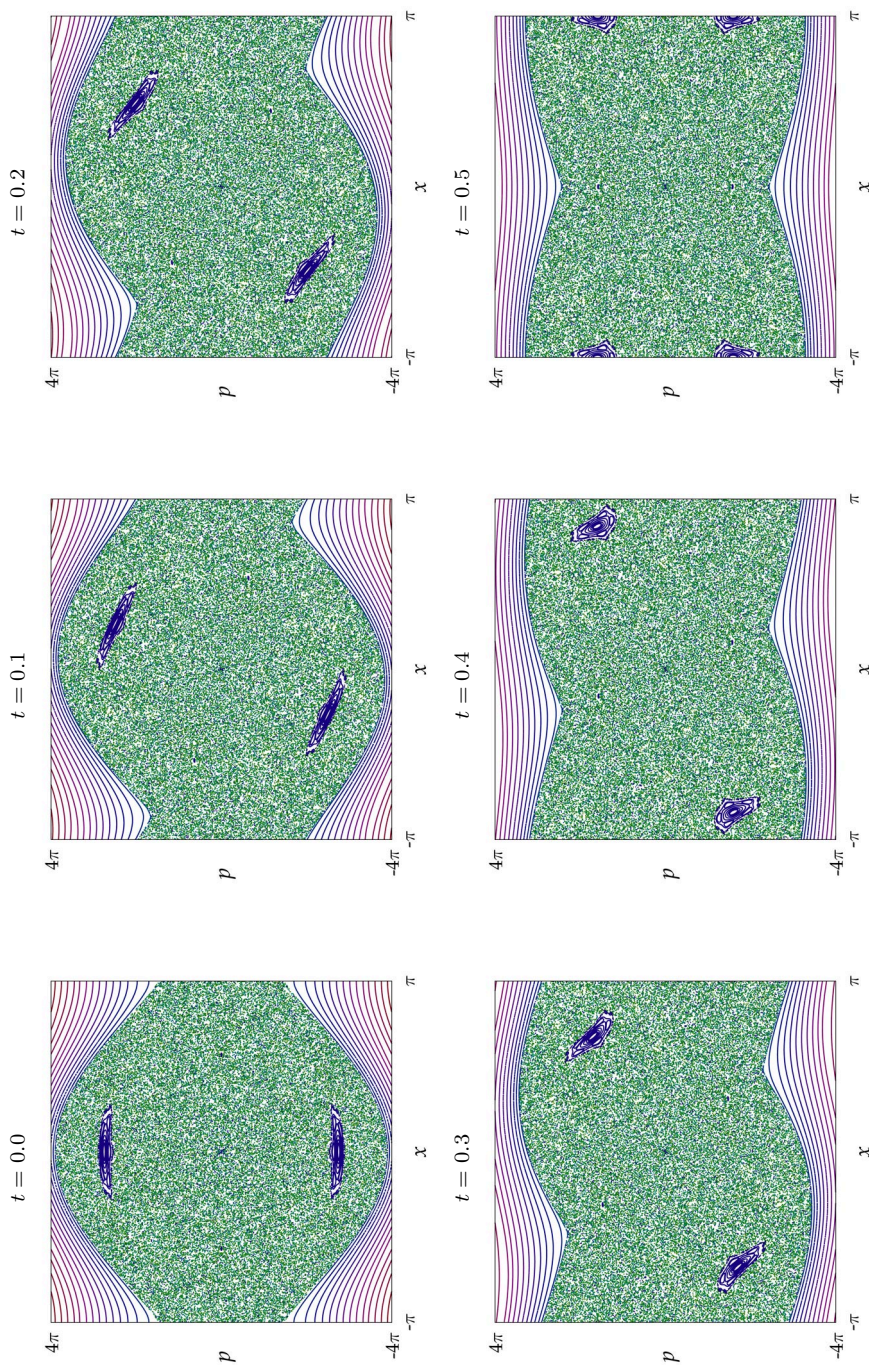
Figure 6.28: Classical phase space (for $\alpha = 10.5$), shown with different sampling phases in the first half of a modulation period. At the start of the modulation period, the islands of stability are separated maximally in momentum, but move inward as they drift away from $x = 0$, and return to their initial momenta by the end of the modulation period. The two islands always remain separated in momentum, and do not cross the $p = 0$ axis. The complementary motions of the two islands produce the fast oscillatory motions in Figs. 6.25-6.27.

in the case of $\alpha = 7.7$ and $\bar{k} = 2.08$ (Fig. 6.25). Here, the first part of the tunneling transport takes place in (at least) two steps through the chaotic sea, with the first chunk of probability crossing during the third period of the potential and the second crossing during the fifth and sixth periods of the potential. The population in the chaotic region is also enhanced at the time of maximum tunneling, where the population in the islands appears to jump in the center region for a short time (during the tenth modulation period). Similar behavior is evident for $\alpha = 11.2$ and $\bar{k} = 2.08$ (Fig. 6.26); in this case, this third oscillation is not as pronounced, but is still present. The details of this oscillation in the chaotic region are also slightly different than in the previous case. This is especially true at the moment of maximum tunneling, where the atoms are mostly in the two islands (unlike the case before, where the atoms were mostly in the chaotic region), but the chaotic region is populated during the modulation periods just before and after this time. In the case of $\alpha = 10.5$ and $\bar{k} = 1.04$ (Fig. 6.27), this oscillation is less visible because of the poorer signal/noise ratio (notice that the atoms are spread over a much larger region in momentum for this value of $\bar{k}$, resulting in an effectively smaller signal). Nonetheless, the tunneling again proceeds in chunks, with the transport visible as faint ridges crossing the chaotic region, especially near the ends of the first, second, fourth, and fifth modulation periods. The tunneling here in some sense resembles a Landau-Zener crossing [Zener32], because the population crosses between the islands at the times of closest approach.

This appearance of probability in the chaotic region during the tunneling is precisely the behavior expected from the picture of chaos-assisted tunneling of [Tomsovic94; Tomsovic01] that we mentioned above, where tunneling occurs as parts of the wave packet break away from the initially populated island, transport through the chaotic sea, and then reassemble in the symmetric destination island. We also recall from the analysis of the three-level model (6.15) of chaos-assisted tunneling that near the center of the avoided crossing, the tunneling rate is given by the splitting(s) between the odd-parity regular state taken pairwise with each of the two even-parity (regular/chaotic hybrid) states, which is of the order $\beta/2$. On the other hand, it is the beating between the two hybrid states that determines the appearance of population in the chaotic region, and this beating occurs at a rate of order β. Thus, we expect the oscillation of

population to be substantially faster than the tunneling oscillation. The oscillations observed in the experiment do not appear to occur with a single frequency, so it may be necessary to include couplings to other chaotic states in order to account more accurately for this phenomenon.

6.4.6 Transport in the Strongly Coupled Regime

For even larger α than we have considered so far, the two symmetry-related islands of stability disappear, and the quantum transport undergoes a transition to qualitatively different behavior than the above tunneling. This strongly coupled behavior is illustrated in Figs. 6.29 and 6.30, where the momentum-distribution evolution is shown (sampled on a fine time scale) for two large values of α. For $\alpha = 17.0$ (Fig. 6.29), the three primary resonances have disappeared, leaving a chaotic region with only very small stable structures, while for $\alpha = 18.9$ (Fig. 6.30),
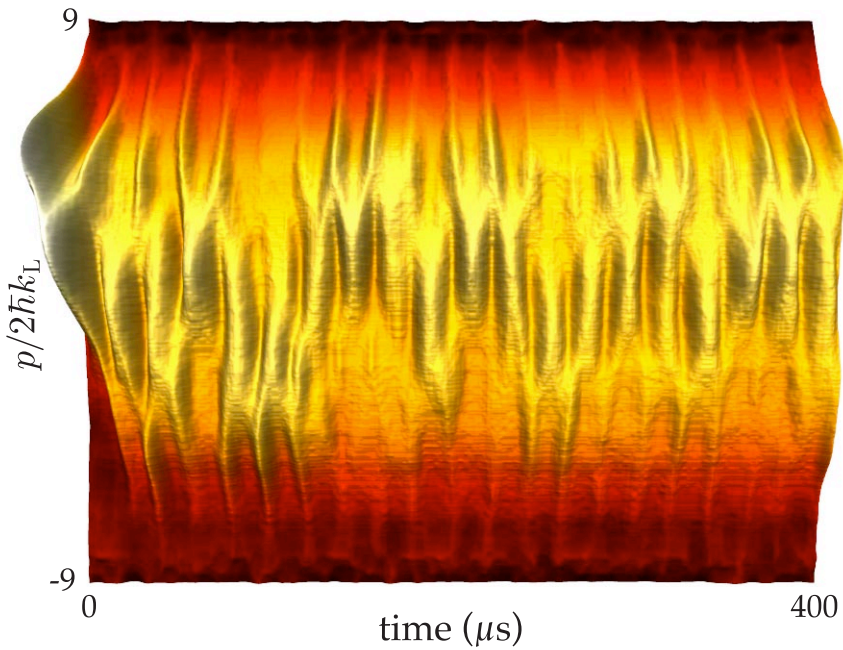

Figure 6.29: Experimental momentum-distribution evolution of chaos-assisted tunneling for $\bar{k} = 2.08$ ($T = 20$ μs) and $\alpha = 17.0$. The distribution was sampled every 2 μs out to 400 μs. The three primary islands of stability have dissolved into the chaotic region in the classical phase space for this value of α (see Appendix C). The experimental momentum distributions show erratic oscillations in time. These distributions were averaged over 10 iterations of the experiment.

there is a small island at the center of the phase space (see Appendix C). The experimental measurement shows erratic oscillations of the momentum distributions on a faster time scale than the tunneling observed above.

We can also understand this behavior qualitatively in terms of the Floquet states of the system. For very small α, the Floquet spectrum consists of nearly degenerate doublets associated with KAM tori, and as α increases the doublets break apart as their associated invariant structures become unstable [Utermann94; Kohler98]. In the regime that we consider here, where the stable structures have disappeared, the splittings are on the order of the mean level spacing [Kohler98] due to level repulsion of the states in the chaotic region [Haake01]. This behavior of the splittings is apparent in the spectra in Figs. 6.23 and 6.24. The Floquet states are no longer well localized in this regime, and thus the initial condition excites several states. The observed behavior is the result of complicated beating between the various populated states,
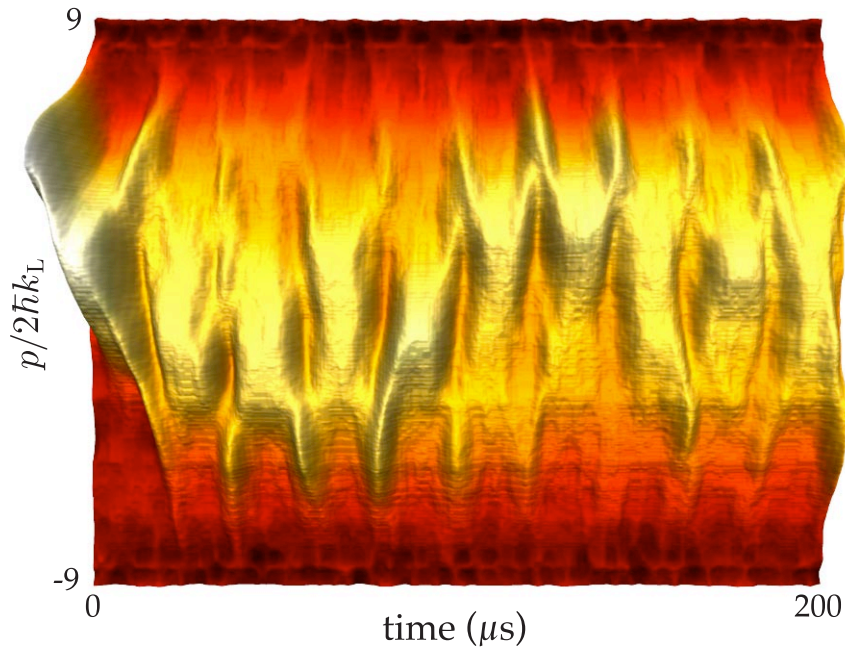

Figure 6.30: Experimental momentum-distribution evolution of chaos-assisted tunneling for $k = 2.08$ ($T = 20$ μs) and $\alpha = 18.9$. The distribution was sampled every 1 μs out to 200 μs. The two outer islands of stability are not present in the chaotic region in the classical phase space for this value of α (see Appendix C). The experimental momentum distributions show erratic oscillations in time. These distributions were averaged over 5 iterations of the experiment.

and we expect a time dependence that is faster than the tunneling due to the relatively large splittings involved.

6.5   Noise Effects on Tunneling

The tunneling that we have described here is obviously an effect of quantum coherence, and tunneling in classically chaotic systems is expected to be suppressed by dissipation [Grobe87; Kohler98], measurement [Sanders89], and noise [Grossmann93]. Here we consider the effects of a noisy perturbation of the optical-lattice intensity, so that the atomic center-of-mass Hamiltonian becomes

$$H = \frac{p^2}{2} - 2\alpha[1 + \varsigma(t)]\cos^2(\pi t)\cos(x) \ , \tag{6.22}$$
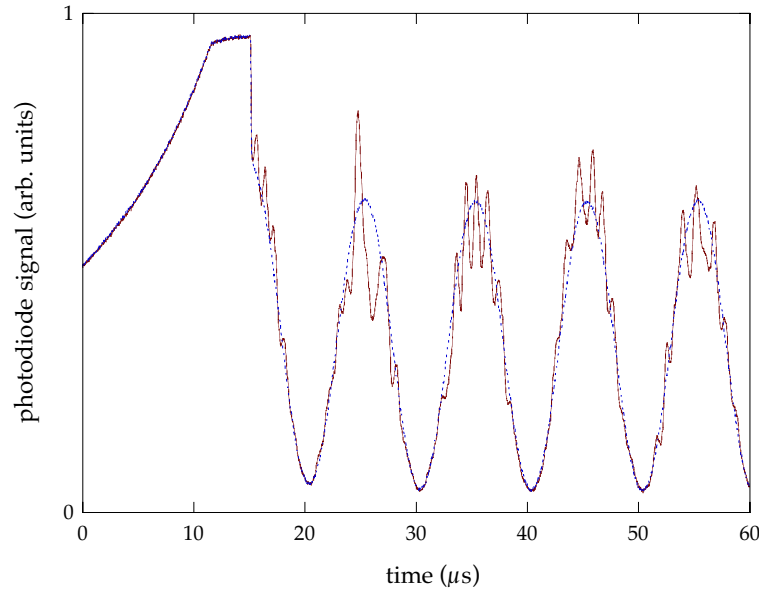

Figure 6.31: Illustration of amplitude noise applied to the optical lattice intensity, as measured by a fast photodiode. The end of the SPASM state-preparation sequence is visible at the beginning of the traces, where the lattice is ramped up and then remains at a high level for several μs after the lattice phase is shifted. The sinusoidal modulations begin immediately after the state preparation, and both the zero (dashed line) and 15.7% (solid line) rms deviation cases are shown here. The noise effects are most pronounced when the lattice is at the highest average intensity because the noise deviation is always proportional to the local average intensity. These traces correspond to the experimental settings for $\bar{k} = 1.04$, where the modulation period is 10 μs, and the noise is filtered with a 1 MHz cutoff frequency.

where $\varsigma(t)$ is a randomly fluctuating quantity with a probability distribution peaked at and symmetric about zero. This noise signal was generated digitally by picking normally distributed random deviates with a 10 MHz sampling rate. The noise was then bandwidth-limited by a digital Chebyshev low-pass filter (see Section 6.5.1) before being applied to the AOM control signal. The cutoff frequency (0.5 MHz for the $\bar{k} = 2.08$, 20 μs modulation period data, and 1 MHz for the $\bar{k} = 1.04$, 10 μs modulation period data) was selected to be well within the 10 MHz modulation response of the AOM driver and to make the noise spectrum the same in scaled units for different modulation periods. The rms noise levels $\langle \varsigma^2(t) \rangle^{1/2}$ that we quote correspond to the noise levels after the low-pass filter. Because the instantaneous noise level is proportional to the mean intensity, truncation effects due to noise deviations falling outside the dynamic range of the laser were rare except in the largest noise case that we consider here (62% rms). An example of the optical lattice intensity for one particular realization of the noise is illustrated in Fig. 6.31.

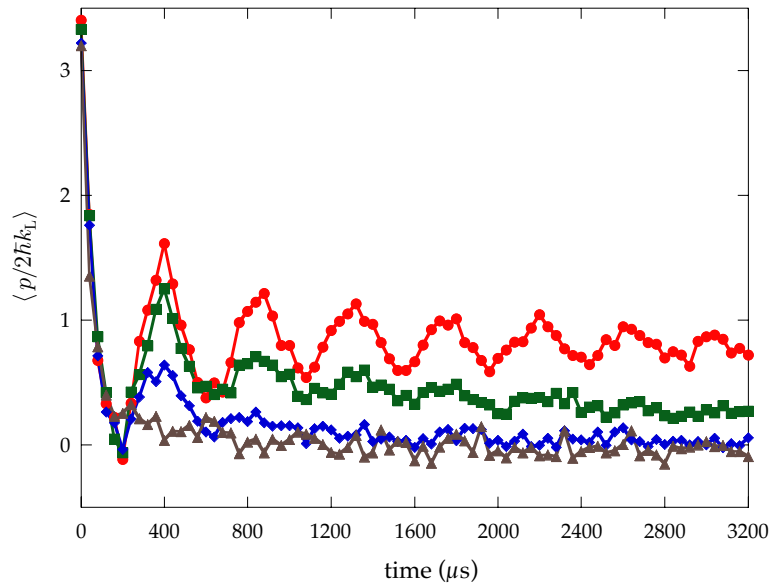The response of the tunneling oscillations to the noise is illustrated in Fig. 6.32 for

Figure 6.32: Effects of applied amplitude noise on the tunneling oscillations for $\alpha = 11.2$ and $\bar{k} = 2.08$. The rms noise levels are 0% (circles), 15.7% (squares), 31% (diamonds), and 62% (triangles). The tunneling is only completely suppressed at the 62% level, and thus is substantially less sensitive than in the $\bar{k} = 1.04$ case in Fig. 6.33. The data were averaged over 10 realizations of noise, and were sampled every 2 modulation periods.

$\bar{k} = 2.08$ and 6.33 for $\bar{k} = 1.04$ ($\alpha = 11.2$ in both cases). As one might expect, the oscillations
are destroyed as the noise level increases, causing damping of the oscillations on progressively
shorter time scales. At the largest levels of noise, classical-like behavior (with noise) is recov-
ered, in that the tunneling oscillations are suppressed. The noise also has the "direct" effect of
causing relaxation to $p = 0$, because the noise permits transitions, both quantum and classical,
out of the initial island of stability and into the chaotic sea. The more interesting feature of
this data, though, is that because the value of α is fixed between the two measurements and
the tunneling periods are approximately the same (in scaled units), we can compare the sensi-
tivity of the system to the noise for two different values of $\bar{k}$. From the data we see that the
tunneling oscillations are suppressed at a much lower level of noise for the $\bar{k} = 1.04$ case than
in the $\bar{k} = 2.08$ case (31% vs. 62% rms). Recalling that $\bar{k}$ is the dimensionless Planck constant
in scaled units, this comparison indicates that the tunneling in this system is more sensitive to
decoherence as the system moves towards the classical limit (i.e., to a larger action scale com-
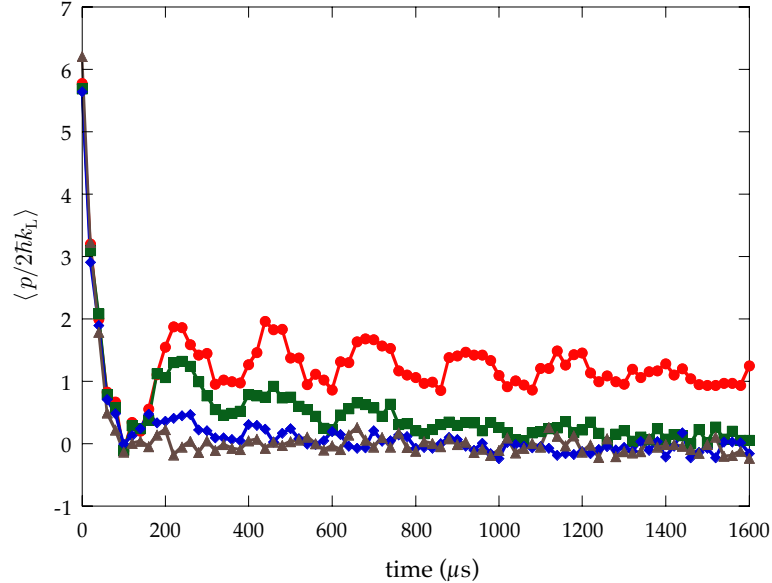

Figure 6.33: Effects of applied amplitude noise on the tunneling oscillations for $\alpha = 11.2$ and
$\bar{k} = 1.04$. The rms noise levels are 0% (circles), 7.9% (squares), 15.7% (diamonds), and 31%
(triangles). The tunneling is completely suppressed at the 31% level, and thus is more sensitive
than in the $\bar{k} = 2.08$ case in Fig. 6.32. The data were averaged over 10 realizations of noise, and
were sampled every 2 modulation periods.

pared to $\hbar$). This behavior is consistent with theoretical expectations, because for smaller $\bar{k}$, the phase-space structure in chaotic systems saturates on a smaller scale [Zurek01], thus being more easily influenced by decoherence (which causes diffusion in phase space). Related experimental results have demonstrated that Schrödinger-cat superposition states in the phase of a cavity field [Brune96], in an atom interferometer [Chapman95; Kokorowski01], and in an ion trap [Turchette00; Myatt00] are more sensitive to decoherence when the separation of the components of the state increases (i.e., as the spacing of the interference fringes decreases). The present experimental results are of a fundamentally different nature, though: while these other experiments study the decoherence of a superposition state produced by some state-preparation method, the interferences in the tunneling here are generated dynamically in this nonlinear system. It is also interesting to notice that since the applied noise here leads to a fluctuating force and thus to diffusion of the atomic momenta, this form of noise mimics a continuous measurement of the atomic positions [Dyrting96; Bhattacharya01]. Thus, we might expect that the system may be more sensitive to noise that mimics a measurement of the atomic momentum, which would cause diffusion of the atomic position, rather than the momentum.

6.5.1   Chebyshev Filter Response

To more completely characterize the noise used in the experiment, we give a description of the filter applied to the noise before it was used to control the optical-lattice intensity. The low-pass Chebyshev filter is specified in terms of three parameters: the cutoff frequency ω_c, the order N, and the passband ripple parameter ε. The frequency response of this filter is specified by the locations of the N poles in the complex s-plane,

$$s_k = -\sinh(v_0)\cos\left(\frac{k\pi}{2N}\right) - i\cosh(v_0)\sin\left(\frac{k\pi}{2N}\right) \quad, \tag{6.23}$$

where

$$v_0 = \frac{\sinh^{-1}(1/\varepsilon)}{N} \quad, \tag{6.24}$$

for $k = (1-N), (3-N), \ldots, (N+1)$ [Parks87]. Thus the complex frequency-transfer function can be written as

$$F(s) = \eta \prod_k \frac{1}{s - s_k} \quad , \tag{6.25}$$

where $s = -i\omega/\omega_\mathrm{c}$, and η is a normalization factor. The (normalized) squared modulus of the frequency-response function is then [Parks87]

$$|F(s)|^2 = \frac{1}{1 + \varepsilon^2 C_N^2(\omega/\omega_\mathrm{c})} \quad , \tag{6.26}$$

where

$$C_N(\omega) = \cos(N \cos^{-1}(\omega)) \tag{6.27}$$

is the Nth-order Chebyshev polynomial. Thus, the normalization factor can be written as $\eta = (\prod_k s_k)/\sqrt{1 + \varepsilon^2 \cos^2(N\pi/2)}$. The passband ripple is also commonly specified in terms of another parameter a, which is expressed in terms of ε as

$$a = 10 \log(1 + \varepsilon^2) \quad , \tag{6.28}$$
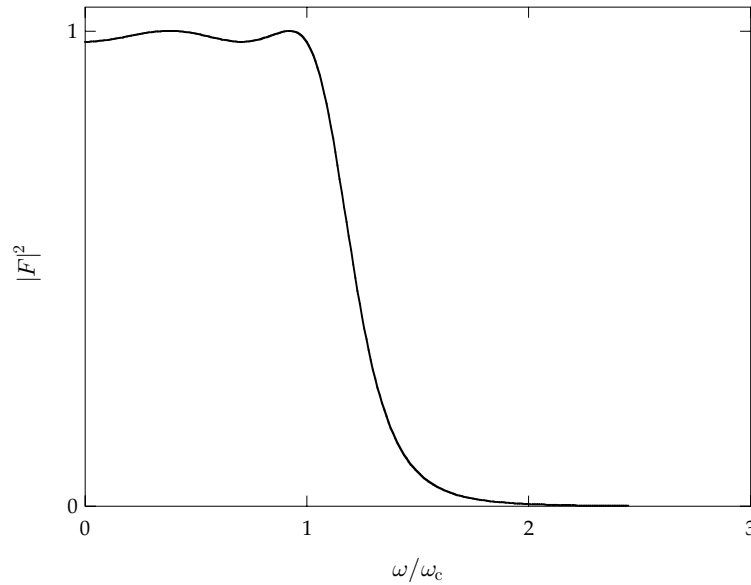
if a is quoted in (positive) dB.

Figure 6.34: Plot of the frequency (power) response function $|F|^2$ of the digital Chebyshev filter used in the experiment, with order $N = 4$ and 0.1 dB passband ripple.

In the experiment, a white noise series (i.e., a series of independent, normally distributed, random deviates) was generated at the 10 MHz sampling rate of the Agilent 33250A waveform synthesizer that controlled the 1D optical lattice intensity. To avoid unattainably large deviations, the Gaussian distribution of these deviates was truncated beyond three standard deviations. The waveform was then filtered using the built-in function in LabView. For the $\bar{k} = 1$ (10 μs modulation period) case, the 1 MHz cutoff frequency resulted in an effective reduction of the rms deviation of the waveform by a factor of about 0.4965. To produce equivalent noise levels in the $\bar{k} = 2$ (20 μs modulation period) case, where the cutoff frequency was 500 kHz, the noise level was first multiplied by $\sqrt{2}$, thus compensating for the different ratio of the sampling frequency to the cutoff frequency.